Understanding the Effects of Environmental Exposure on Surface Related Properties of Graphene, Graphite, and Rare Earth Oxides

by

Muhammad Ghassan Salim

Bachelor of Science, University of Pittsburgh, 2012

Master of Science, University of Pittsburgh, 2015

Submitted to the Graduate Faculty of the

Dietrich School of Arts and Sciences in partial fulfillment

of the requirements for the degree of

Doctor of Philosophy

University of Pittsburgh

2019

UNIVERSITY OF PITTSBURGH

DIETRICH SCHOOL OF ARTS AND SCIENCES

This dissertation was presented

by

Muhammad Ghassan Salim

It was defended on

March 27, 2019

and approved by

Dr. Alexander Star, Professor, Department of Chemistry

Dr. Hernandez Sanchez, Assistant Professor, Department of Chemistry

Dr. Lei Li, Associate Professor, Department of Chemical and Petroleum Engineering

Dissertation Advisor: Dr. Haitao Liu, Associate Professor, Department of Chemistry

Understanding the Effects of Environmental Exposure on Surface Related Properties of Graphene, Graphite, and Rare Earth Oxides

Muhammad Ghassan Salim, Ph.D.

University of Pittsburgh, 2019

There is a good understanding of surface chemistry in vacuum, but not for materials in real environments. Fully understanding the surface properties of materials in ambient environment plays an important role in realizing their potential applications toward other fields of chemistry. This dissertation focuses on how the environment alters the surface chemistry and properties of different materials. My work has three parts: graphitic carbon, rare earth oxides, and graphene fibers. Various surface analysis techniques are utilized to investigate and characterize the relevant surface properties of carbon and rare earth oxide materials and their contaminations due to exposure in real environments. Results from such work is further used to probe and manipulate the effect of surface chemistry on the adhesion chemistry of graphene fibers, ultimately changing its respective mechanical properties.

Table of Contents

List of Tables

List of Figures

List of Equations

Abbreviations

AFM	Atomic Force Microscopy
ALD	Atomic Layer Deposition
ATR	Attenuated Total Reflectance
AMC	Airborne Molecular Contaminant
BE	Binding Energy
CNT	Carbon Nanotube
CVD	Chemical Vapor Deposition
FTIR	Fourier-transform Infrared Spectroscopy
HOPG	Highly Ordered Pyrolytic Graphite
KPFM	Kelvin probe force microscopy
MWCNT	Multi-walled Carbon Nanotube
PES	Photoelectron Spectroscopy
PMMA	Poly(methyl methacrylate)
REO	Rare Earth Oxide
SCC	Stress Crack Corrosion
SEM	Scanning Electron Microscopy
SWCNT	Single-walled Carbon Nanotube
UHV	Ultra-High Vacuum
UPS	Ultra-violet photoelectron spectroscopy
UT	Uniaxial Tensile
VOC	Volatile Organic Compound
WCA	Water Contact Angle
XPS	X-ray Photoelectron Spectroscopy

Preface

Foremost, I would like to express my upmost sincere gratitude toward my research advisor, Professor Haitao Liu. I am sincerely grateful for his time and guidance during my PhD. The ways and means that Haitao operates his group provides an ideal scenario for fostering innovation and developing new ideas toward advancing associated fields of science. His ability to encourage, while providing insightful advice, has led to making my Ph.D experience rewarding and productive.

I am also very grateful to Prof. Lei Li and Prof. Tevis Jacobs for providing the opportunity of doing some of my research in each of their labs for many years. Their insightful comments and engineer's perspectives expanded my point of view on many collaboration projects.

I would like to thank my master's thesis committee members, Prof. Haitao Liu, Prof. Alexander Star, and Prof. Jill Millstone for their time and suggestions on my exam and thesis writing. Additionally, I would like to thank Prof. Alexander Star, Prof. Hernandez Sanchez, and Prof. Tara Meyer for their advice and guidance through the course of my proposal writing.

Furthermore, I would like to express my sincere appreciation for my Ph.D. thesis committee members, Prof. Haitao Liu, Prof. Alexander Star, Prof. Hernandez Sanchez, and Prof. Lei Li for contributing their time and support.

I would like to also give my full gratitude to my past and present colleague members and collaborators. Special thanks go to Dr. Zhiting Li, Dr. Feng Zhou, and Dr. Andrew Kozbial for their generous assistance for when I first started my research; to Justin Hurst, Mina Kim, Luke Thimons, and Nathan Tolman for all of our thorough problem-solving conversations, as well as helpful assistance and suggestions; to my undergraduate researchers Michelle Montgomery and

Brennan Carr for their time and dedication; to Dr. Joel Gillespie for building up and maintaining excellent ESCA instrumentation; and to Dr. Ericka Huston for her kind generosity, friendship, advice, and assistance in my endeavors as a teaching fellow. I would also like to cordially thank Dr. Karen Ricardo-Hernandez, Anqing Xu, Christopher Kurpiel, Dr. Kim Hyojeong, Dong Wang, Ruobing Bai, Prof. Shichao Zhao, Dr. Raúl García Rodríguez, Dr. Cheng Tian, and Dr. Liwei Hui, Dr. Peter Bell, and Dr. George Bandik. You are all wonderful friends and scientists, and it has been my pleasure to work with all of you.

Lastly and above all, I would like to express my great gratitude to my parents, Ghassan and Debra Salim, who have supported me and provided me with a comfortable life with sufficient space and opportunities for all of my choices.

1.0 Introduction

1.1 Overview

In early 2016, a *Nature* survey of 1,576 researchers took a brief online questionnaire consisting of reproducibility in research. This survey revealed that 70% of these researchers had tried and failed to reproduce other scientists' published experiments. When work does not reproduce, it is assumed that there is a perfectly valid, and probably very simple, reason as to why; however, it may be the case that the published results are incorrect. Even more so, incentives to publish positive replications are low, and journals are even more reluctant to publish negative findings. Several of the survey respondents who did publish a failed replication, stated that they were forced to downplay comparisons with the original publication.[1] The question arises, if this crisis is valid or if it's just perceived by researchers as a fault due to mismanagement or the review process.

The foundation of my work originates from an example of irreproducible results in literature. In 2013, Li et al. revealed that a graphitic carbon surface is actually much more hydrophilic than previously thought.[2] It had been initially believed that a graphene or graphite surface is intrinsically hydrophobic, an observation which had been reproduced numerous times in the past.[3-9] However, Li et al. showed that a pristine graphene/graphite surface is much more hydrophilic and only exhibits hydrophobic behavior upon exposure to the environment (e.g., ambient air).[2] This was the first study to show that graphene and graphite are mildly hydrophilic and become hydrophobic upon exposure to ambient air, due to the adsorption of airborne contaminants. This result was then reproduced many times since its publication in 2013.[10-15] In

this specific case, the discrepancy and irreproducibility of data was due to a simple oversight in the original published works. The issue being that the surface contamination by molecules in the ambient atmosphere was not considered.

The research discussed herein was initiated through another example of published results not being reproducible; the purpose being to highlight results involving rare earth oxides (REOs). The fundamental processes studied through the REO contamination work was analyzed in further detail on graphitic carbon, a substrate which was proven to exhibit a similar time-related adsorption/contamination phenomenon. After completion of this work, the influence of environmental exposure of graphitic carbon on its surface chemistry and adhesion is then used to study the mechanical properties of graphene. The ultimate goal is to lead to understanding the effects of gas-phase contaminant adsorption on different materials properties in real environments.

1.2 Fundamentals in Surface Adsorption

Phenomena taking place at a solid-gas interface is governed by specific and aspecific interactions between the atoms at the solid surface and the molecules approaching the surface from the gas. Adsorbed molecules may accumulate to form monolayer to multilayer structures on a surface, depicted in Figure 1.

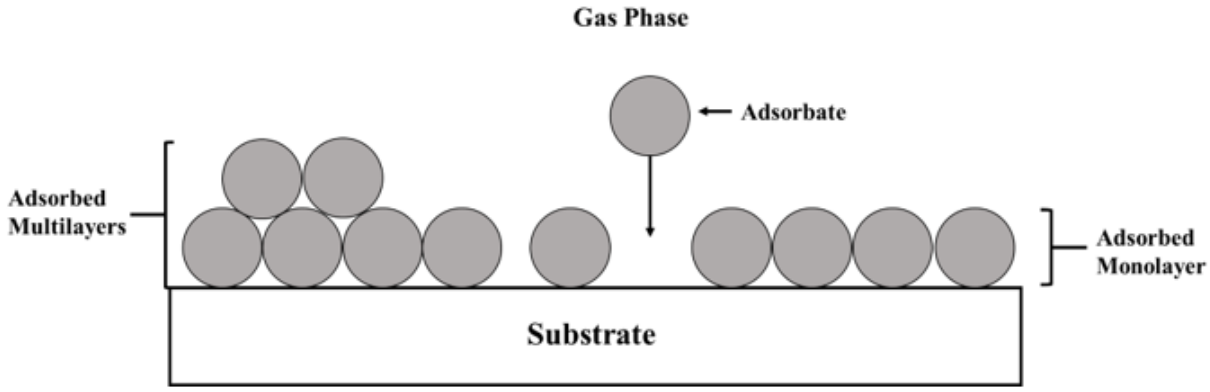

Figure 1. Schematic of adsorption process of gas-phase adsorbates on the surface of a solid material substrate.

Adsorption of probe molecules onto solid surfaces have been used to describe related properties of many solid-gas interface systems. This is accomplished through the implementation of various surface sensitive analytical techniques (e.g., spectroscopic, thermoanalytical, physical etc.). Adsorption takes place at active surface sites, specific points on the solid surface which possess an affinity toward the gas-phase adsorbate and occurs when this attractive interaction is strong enough to overcome the disordering effect of thermal motion.[16-17] In this sense, adsorption is a spontaneous exothermic process, whether it be physisorption or chemisorption.[16, 18]

Adsorption kinetics have been described through isotherms connecting characteristic functions of the gas adsorbate, solid surface, and other environmental properties.[7, 18-19] However, deviations from these models are observed in real systems due to many interactions unaccounted for by such equations, including but not limited to: interactions between adsorbates, heterogeneous surfaces, and changes to the chemistry of the adsorption sites.[17, 20] These deviations compound as the composition of participating gas and surface components becomes more complex, where competitive adsorption results in dynamic, time-related, changes on surface chemistry. In this

sense, the adsorption selectivity of surfaces in multi-gas mixtures changes over time of exposure to the gasses—a function of energetic, kinetic, and steric adsorption considerations. Silicon wafers have shown to exhibit such correlation and competition in bi- and multi-component gaseous mixtures. This phenomenon can be related to ambient air conditions, where the number of gas molecular components is greatly increased. [17, 21-22]

1.3 Adsorbates in Real Environments

After an initial report by IBM researchers in 1990, which discussed the detrimental effects of cleanroom airborne molecular contaminants(AMCs), the semiconductor industry began to examine the damage and controls during related manufacturing processes.[23-24] AMCs refers to molecules in the air which lead to surface contamination. In accordance with ISO 14644-8, the classification of these contaminants are molecular substances in the gaseous or vapor state that may have deleterious effects on products, processes, or equipment in a cleanroom or controlled environment. One constituent of this group is volatile organic compounds (VOCs).

The term VOCs covers a broad spectrum of saturated, unsaturated, and other substituted carbon molecules. In a laboratory, or cleanroom, the organic compounds which may be present in the atmosphere typically originate from multiple sources such as chemical solvents, pump oil vapor, or even the outgassing of building materials.[25-29] As an example, the concentration of plasticizer emission from vinyl flooring is on the $\mu g/m^3$ (ppb) level. The majority of VOCs found in a laboratory or cleanroom environment have been measured to be in concentration range of ppt to ppm.[27-28] The quantity of organic compounds outgassed from materials is dependent upon surface area, outgassing time, surface and atmospheric chemistry, and other environmental

properties (e.g., pressure, temperature, etc.). Ultimately, the particular exposure conditions of a pristine surface to AMCs influences composition and dynamics of surface contamination.[17] Characterization of these contaminants is of upmost importance in order to understand their effects and implications towards surface-sensitive applications of materials.

1.4 Characterization of Surface Contaminants

This section will briefly discuss the general operation principles and interpretations of data for surface characterization techniques used in my studies. The specific measured influences of contamination by these related surface-sensitive techniques are discussed further in later sections **(2.0; 3.0)**, with a focus on the purpose for which they are being implemented. The techniques discussed include water contact angle (WCA), spectroscopic ellipsometry, and photoelectron spectroscopy (PES).

1.4.1 Water Contact Angle

To study the surface energy of a material, WCA measurements are applied to describe a surface as hydrophobic or hydrophilic. When a drop of water deposited on a solid it will contact the substrate in a disc of radius ℓ. As shown in Figure **2,** at the edge of the droplet there is an observable angle θ, which arises from interactions at the solid, liquid, and vapor interfaces. The Young's equation is used to determine the static equilibrium of these interactions (Eq. 1), where

the equilibrium contact angle θ is determined by the liquid-solid interface energy γ_{SL}, the solid-vapor interface energy γ_{SV}, and the liquid-vapor interface energy γ_{SL}, depicted in Figure 2.[30-31]

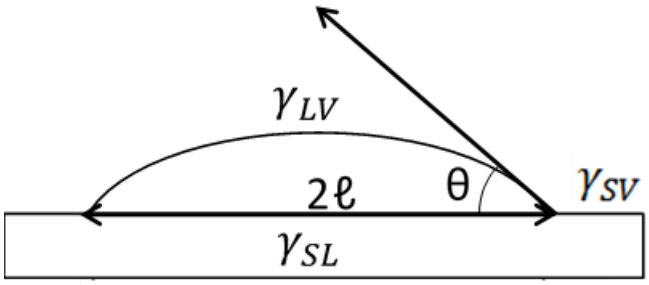

Figure 2. Contact Angle. Schematic of the forces taking place on a droplet of water residing on a surface, which play a role in determining the resulting contact angle θ.

Equation 1. WCA

$$\cos(\theta) = \frac{\gamma_{SV} - \gamma_{SL}}{\gamma_{LV}}$$

Generally, when a liquid droplet is placed onto a solid surface, its behavior depends on the adhesive forces between the liquid and the surface. For a hydrophilic surface, the adhesive forces are attractive so that the liquid drop is pulled toward the surface and spreads out to increase the contact, resulting in a small water contact angle (< 90˚). In contrast, a hydrophobic surface usually shows repellent forces towards the water drop, which beads up (> 90˚) in order to minimize its contact with the solid surface.

1.4.2 Spectroscopic Ellipsometry

Spectroscopic ellipsometry is a well-established optical technique for the determination of optical constants and thickness of thin films. Due to its surface sensitive and non-destructive properties, this technique has been widely used in many application fields such as semiconductor, photovoltaics, optoelectronics, biotechnology and surface coatings, etc.[32]

In ellipsometry, p- and s-polarized light waves are reflected from a sample surface. Two values are ultimately measured by this technique, (ψ, Δ) which represent the amplitude ratio ψ and phase difference Δ between the p- and s-polarizations. The amplitude ratio ψ is characterized by n (refractive index), while Δ represents light absorption described by k (extinction coefficient) or the absorption coefficient α. The ellipsometry parameters (ψ, Δ) are defined by the amplitude reflection coefficients for p-polarization (r_p) and s-polarization (r_s), Eq. 2.[32-33]

Equation 2. Ellipsometry

$$\boldsymbol{\rho = \tan(\psi)\, e^{i\Delta} = \frac{|r_p|}{|r_s|}}$$

Thus, the two values (n, k) can be determined directly from the two ellipsometry parameters (ψ, Δ) obtained from a measurement. In other words, in ellipsometry, the optical constants (n, k) are determined by characterizing the polarization change upon light reflection.[32-33]

In this work, ellipsometry is applied to detect the accumulation of airborne AMCs adsorbing onto a surface, which is usually in the sub-nanometer range. This technique enables a

nondestructive, efficient and highly sensitive detecting over an extended time scales to visualize AMC adsorption.

1.4.3 Photoelectron Spectroscopy

PES has been established as one of the most important and extensively used methods to study the electronic structure of molecules, solids, and surfaces by providing atomic and molecular information on a surface. With regards to VOC contamination, PES is used to detect and quantify the atomic presence and related molecular bonding chemistries of associated contaminants. Adsorption of VOC contaminants onto a surface is associated with a detectable increase of electron counts at binding energies associated to carbon and/or oxygen, the primary elemental components of VOCs.

During PES, photons from a monochromatized radiation source are directed towards a sample, whereby photoelectrons liberated by the photoelectric effect are analyzed with respect to emission angle and kinetic energy by an electrostatic analyzer through Eq. 3.[34-35]

Equation 3. PES

$$\mathbf{E_b = h\nu - E_{kin} - \phi}$$

Where the E_b is the binding energy of an emitted photelectron, hν is the photon energy, E_{kin} is the kinetic energy of the emitted photoelectron, and ϕ is the work function associated with the sample surface. In a laboratory setting, a wide range of photon energies can be used for photoexcitation. The two different excitation sources utilized in my work (40.6eV, He II and 1486.6 Al-Kα) in order to selectively target either valence or core electrons, each providing

different depth, atomic, and bonding information. A schematic of the principle setup of a photoelectron spectrometer is shown in Figure 3.[34-35]

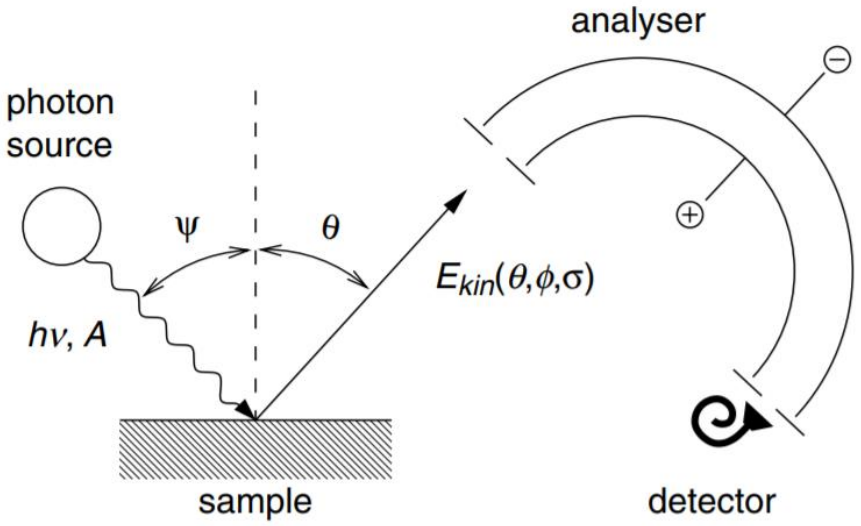

Figure 3. Monochromatic photons with energy hν and polarization (*A* is the vector potential of the electromagnetic field) hit the sample surface at an angle ψ with respect to the surface normal. The kinetic energy E_{kin} of the photoelectrons can be analyzed by use of electrostatic analyzers as a function of the experimental parameters (e.g. emission angle (θ, φ)) the electron spin orientation σ, or the photon energy or polarization. The setup is evacuated to ultra-high vacuum (UHV), typically at a set point of $1x10^{-10}$ mBar.

1.5 Contamination Effects on Surface Related Applications

On the broad scale of adsorption, control and cleanliness are the primary concerns. This is especially the case in the semiconductor industry—where performance, reliability, and fabrication processing are all significantly impacted by even extremely low levels of surface contamination. The magnitude and kinetics of this contamination-induced surface property alteration is sensitive to the chemical nature and compositions of the substrate, adsorbates, and the environmental properties.

1.5.1 Effects of Airborne Contamination on Graphene/Graphite

It is well known that surface adsorption of airborne contamination, particularly VOCs, increases its relative hydrophobicity, which is measured by an increased WCA. For graphene/graphite this occurs within seconds of air exposure.[2] This behavior has also been observed to occur for many other metal oxides and metals, although the exact timescale of WCA evolution changes between materials.[36] Given the rapid kinetics of the airborne contamination, it should then be expected that a wide range of surface properties would also be affected by this phenomenon. Any interfacial properties that are dependent upon the surface energy, dielectric properties, or chemical reactivity have the possibility of being influenced by the airborne adsorbates.

Zou et al. showed that freshly exfoliated highly oriented pyrolytic graphite (HOPG) has a higher double layer capacitance (6.0 $\mu F/cm^2$) than that of HOPG aged in air for 24 h (4.7 $\mu F/cm^2$).[37] Hurst et al. also showed that exposing a freshly exfoliated HOPG surface to ambient air and 1-octadecene vapor (*ca.* 1 ppm) caused a *ca.*30% and 70% decrease in its double layer capacitance,

respectively.[38] Studies on the heterogeneous electron transfer rates of chemical vapor deposition(CVD)-grown graphene can be very high if fabricated without using conventional polymer transfer techniques. The rate constants are 2-3 orders of magnitude higher than those fabricated with poly(methyl methacrylate) PMMA for graphene transfer. This is attributed to the presence of surface contaminants (residual PMMA).[39] Nioradze et al. showed that the electrochemical activity of HOPG basal plane surface can be significantly lowered, 3-6 orders of magnitude, by the adsorption of organic contaminant impurities from both air and ultra-pure water.[40] Although the effects of these contaminants have been studied, there has been no thorough study of the adsorption kinetics or composition. Therefore, it is of great interest to fully characterize the coverage and chemical nature of this airborne surface contamination, since the composition of contamination plays a key role on sensitive surface measurements. This is presented in section **3.0.**

1.5.2 Implications of Surface Adsorbates on Mechanical Properties

Carbon nanotubes (CNTs), which can be structurally compared to rolled graphene sheets, and when dispersed in polymer or metal matrices, have been shown to reinforce and enhance the mechanical properties of the matrix in which displaced.[41] However many of these reinforcement prospects are limited by restrictions that arise from the fabrication process of the nanofibers.[42-48] One example of these restrictions are the low surface-to-volume ratios, which is a result of inaccessibility to the inner walls of the nanotubes. These interactions prevent access to the interlayer space within the nanotube, limiting elasticity and strength.[43] One symptom of this inaccessibility is poor dispersion and high aggregation in polymer matrices, which has been observed for multi-walled carbon nanotubes (MWCNTs) in epoxy matrix.[49]

Smaller diameter CNTs have increased interlayer spacing, due to repulsive forces encountered via increased curvature. The Van der Waals forces between CNT layers in MWCNTs result in inward force on the center-most tubes, which leads to a small critical axial strain, when compared to the single-walled carbon nanotube (SWCNT) variant. Additionally, a common defect in MWCNTs is the capping of its ends. This defect prevents access to the intra-layer space between the CNTs , which typically leads to a decreased overall strength due to poor load transfer between layers (since it is inaccessible to additives, such as a polymer matrix).[41-42, 44] Access to the intralayer spacing is also vital for maximizing elasticity by reducing intralayer interactions, such as VDW forces.

Comparisons of bending stiffness and in-plane stiffness values between SWCNTs and MWCNTs species led to important conclusions about the effect of added layers on nanotube strength. The in plane bending stiffness, or resistance to bending, of a CNT increased as the number of nanotube layers increased.[45-48] Additional tensile strength measurements of MWCNTs have implied a flexibility which is improved by a reduction in the interactions between multiple CNT layers. In this sense, the optimization would be to use a single layer of graphene, since graphene-graphene interactions could be decoupled quite easily since there is easy access to the entire surface area. Preventative measures could be taken to block these interactions, leading to an increase in the measured elastic modulus. It has been shown that the elastic modulus of graphite reduces as the number of graphene layers increases, which is attributed to an increase of the total layer interactions.[50-51]

Preventing these interactions, through the incorporation of a contaminant material (e.g., polymer), between interacting areas of the surfaces, has shown to improve the properties of CNTs. The resulting composites have exhibited combination properties of both carbon additive and

matrix. Section **4.0** explores the mechanical properties of a graphene related to layer adhesion issues. This is done by the use of mechanical tensile tests, which is explained below.

1.5.2.1 Tensile Tests

Generally, a tensile test involves subjecting a sample material to tension. The specific type of tensile test used in my work is uniaxial tensile (UT) testing. A simple picture of this is shown in Figure 4, where an axial tension is applied to a mounted specimen by a servo or motor. As the force (F) is increased (measured by the load sensor), axial displacements can be measured by the camera/microscope. This method can ultimately be used to determine a material's elastic modulus (*E*, resistance to elastic deformation) and tensile strength (σ_b, the maximum amount of tensile stress a material can take before failure).

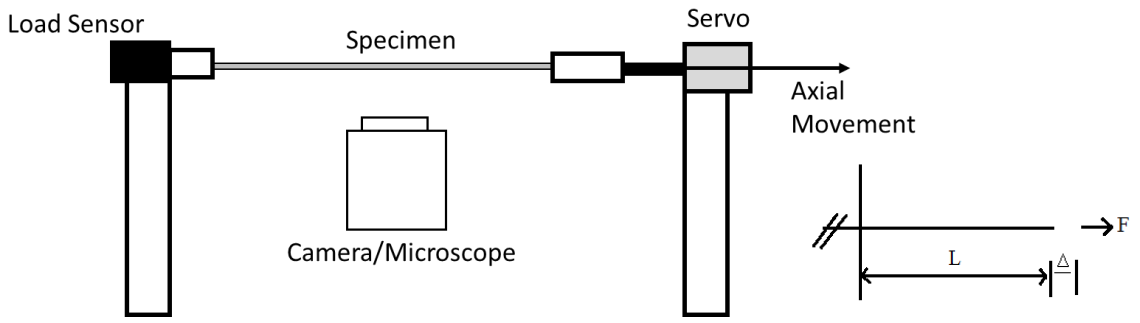

Figure 4. Schematic of a UT testing setup.

As a UT test is performed, the forces measured by the load sensor can be plotted against the axial displacements (ΔL) of the specimen, until the sample breaks at F_{max}. This generates a F- ΔL plot. An example of one is shown in Figure 5, where K is the slope of the linear portion.

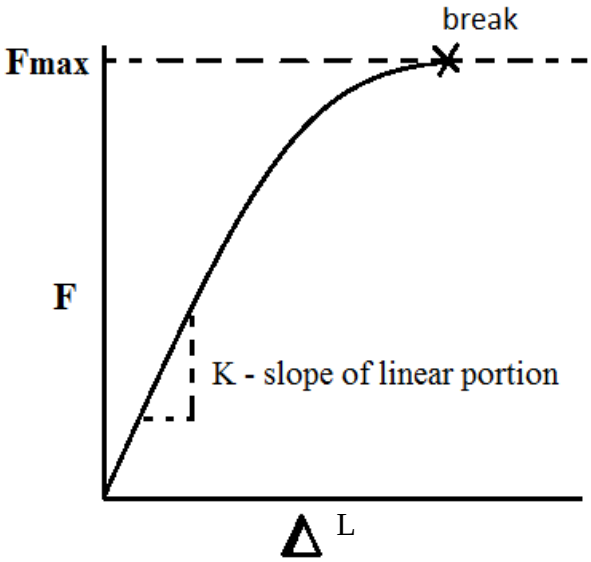

Figure 5. Example of an F- ΔL plot for a UT test. F_{max} corresponds to the force at which the specimin breaks

This plot can then be used to calculate *E* and σ_b of the through equation 4, where L is the initial length and A is the axial cross-sectional area of the sample.

Equation 4. Elastic Modulus and Tensile Strength

$$E = \frac{KL}{A} \; ; \; \sigma_b = \frac{F_{max}}{A}$$

Similarly, a stress (σ)-strain(ε) curve is often used in material science to represent this data. Where σ is the instantaneous force per area and ε is the normalized instantaneous axial deformations during testing, Equation 5. In this case, the linear slope of the stress-strain curve is *E*, the elastic modulus.

Equation 5. Stress and Strain

$$\sigma = \frac{L}{A} \;\; ; \; \varepsilon = \frac{\Delta L}{L}$$

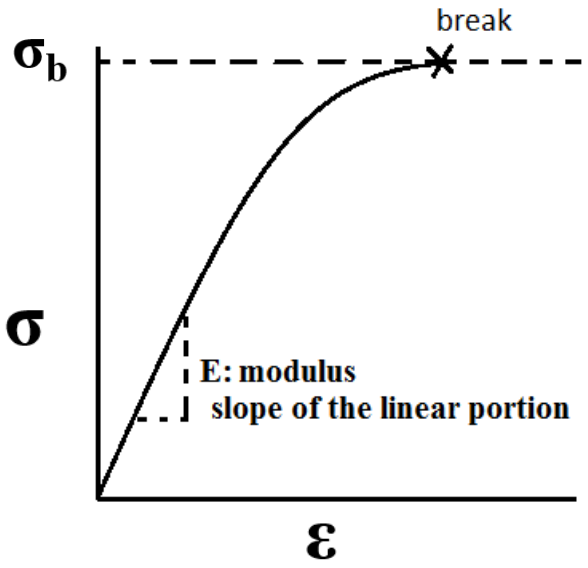

Figure 6. Example plot of stress-strain curve, where *E* is the slope of the linear portion.

2.0 Hydrophobicity of Rare-Earth Oxide Ceramics

2.1 Chapter Preface

Modified segments of the materials in this chapter were submitted as a commentary to *Nature Materials.*

List of Authors: Muhammad Salim, Feng Zhou, Haitao Liu

Author Contributions: M.S. and H.L designed and directed experiments. M.S. and F.Z. conducted the experiments. All authors discussed results and M.S. and H.L. co-wrote the manuscript with input from all authors.

2.2 Background

Many applications require materials that are both intrinsically hydrophobic and robust to harsh chemical environments.[52] The current technology in hydrophobic coating is limited to organic materials that are easily degraded. A study by Azimi *et al.* suggested that REOs are intrinsically hydrophobic because their electronic structure prohibits their bonding with interfacial water.[53] This is a potentially transformative discovery because metal oxides are much more robust than organic coatings and therefore could be used in a much wider range of applications.

Research contained herein was the first submitted work to show that the REO samples used in Azimi *et al.* are likely contaminated by airborne VOCs and such unintentional contamination contributed to their reported hydrophobicity of REO. Our data further showed that a contamination-free REO surface is hydrophilic. Measurements were performed on REO foils and wafers, the latter of which were provided by the researchers from the initial publication, Professor K. Varanasi's group.

The initial submission process of this work to *Nature Materials* required correspondence with Prof. K. Varanasi, to discuss the possible role of airborne contamination on the reproducibility issue for REO data. During this correspondence, a separate study came to similar conclusions as ours.[54] Since then, other independent reports had also arrived to similar conclusions, and challenged the findings of Azimi *et al.*[55-59]

2.2.1 Hydrocarbon Contamination in Azimi *et al.*

VOCs originate from both natural and anthropogenic sources (*e.g.* incomplete combustion) and their concentrations are typically range in the parts-per-trillion to parts-per-billion

level.[60] Airborne hydrocarbons are known to adsorb onto a wide range of surfaces (*e.g.*, Au, TiO_2, SiO_2, and graphene) to result in a universal increase of their WCA and hydrophobicity.[61] The magnitude and kinetics of this contamination-induced wettability change is sensitive to the chemical nature of the substrate and the local environment. *e.g.*, the contamination takes hours to occur on SiO_2 but only minutes for Au.[62-63] As a general rule, one should assume that a high-energy surface is contaminated unless proven otherwise.

Previous studies have shown that REO is a high-energy surface. Taking CeO_2 as an example, multiple experimental measurements and theoretical calculations have reported its surface energy to be around 1 J/cm^2.[64-66] This value is characteristic of a high-energy (*i.e.*, hydrophilic) surface. As a comparison, the surface energy of graphite is about 20 times smaller (*ca.* 55 mJ/cm^2).[67] These results are expected given the high melting point of REOs (*e.g.*, m.p. of CeO_2 is 2400 ^oC), which is indicative of high lattice energies of these materials. Given this rich literature precedence on the hydrophilic nature of the REOs, it is surprising that Azimi *et al.* observed hydrophobic behavior on these materials.

We suspect that hydrocarbon contamination may have occurred on the REO samples used in Azimi *et al.* In that study, the REO samples were stored in a vacuum desiccator before their wettability was tested. Storing samples in a vacuum desiccator could expose them to high level of hydrocarbon emission from vacuum grease, plastic parts (*e.g.*, rubber vacuum hose), and back-diffused pump oil vapor. Although low carbon contents were reported by XPS data in Azimi *et al.*, *such XPS data were collected after the REO surfaces were cleaned by Ar^+ sputtering* and therefore do not support the absence of hydrocarbon contamination.

We could not experimentally verify the degree of sample contamination in Azimi *et al.* The details of sample storage condition (*e.g.*, storage time, vacuum source, and vacuum level) were not

documented in Azimi *et al.*; attempts to obtain such information from Dr. Varanasi were unsuccessful. However, as will be shown below, hydrocarbon contamination even occurs on samples stored in a UHV environment. In addition, a recent paper from Varanasi group also reported *ca.* 12% of carbon contamination on a CeO_2 sample after its storage in a vacuum desiccator.[68] Therefore, it is likely that hydrocarbon contamination have occurred on the REO samples used in Azimi *et al.* and such contamination may have contributed to the hydrophobic behavior they observed on these samples.

2.3 Methodology

2.3.1 XPS

XPS measurements were taken with a Thermo Scientific™ ESCALAB 250Xi. The X-Ray source was monochromatic and generated using an Al-Kα anode (hν=1486.6 eV). The spot size was 0.4 mm with a takeoff angle of 45°. A minimum of 10 scans were performed, with 50 eV pass energy, for each measurement, and analyzed with Thermo Scientific™ Avantage Data System software. Thermally annealed samples were immediately transferred from the annealing furnace to the XPS chamber using a sealable glass container in order to prevent possible adsorption of airborne contaminants. Before transport, the glass container was cleaned with UV-Ozone for 20 minutes and flushed with pure N_2 gas in order to ensure minimal hydrocarbon contamination from the inside surface of the glass. It is important to note that glass joint grease was avoided, as to prevent possible airborne contamination within the transfer container. Transport time of the sample to the XPS preparation vacuum chamber was kept below 5 minutes, with the sample only being in

the XPS preparation at atmospheric pressure for less than one minute before vacuum pumping. XPS measurements were taken after 10 minutes of vacuum pumping. This method provided minimal air exposure to the sample, reducing possible sources of airborne contamination.

Samples aged in UHV were accomplished by storing the samples in the XPS analysis chamber. UHV pressure during storage was at 7×10^{-10} Torr, with the pressure reducing to 3×10^{-8} during measurements.

2.3.2 Water Contact Angle

WCA measurements were conducted using a VCA Optima XE contact angle system at room temperature (22 ^{o}C). Water droplets were 2 μl in size and suspended on the tip of a needle. The sample surface was raised up to carefully touch the bottom of the water droplet. Static contact angle measurements were calculated using the VCA Optima XE software with images the captured by a CCD camera. Each measurement was repeated three times and the average value was reported. REO samples were stored in UV/O_3 cleaned glass vials open to the air and positioned horizontally to minimize any particles from landing directly onto the sample surface.

2.3.3 Surface Morphology Characterization

Four samples of CeO_2 thin film on Si wafers were analyzed using optical microscopy and atomic force microscopy (AFM). One sample was left as-received, while the other three were annealed at 300 ^{o}C, 500 ^{o}C, and 800 ^{o}C. Samples were annealed for 45 minutes at the desired temperature, with a 10 (300 ^{o}C), 15 (500 ^{o}C), and 20 minutes (800 ^{o}C) ramp period, respectively.

2.3.3.1 Optical Microscopy

Optical images were taken using an optical microscope (AmScope) equipped with a digital camera.

2.3.3.2 Atomic Force Microscopy

The AFM measurements were taken using an Asylum MFP3D AFM in AC Air Tapping Mode using silicon tips with a resonance frequency of 320 kHz. Analysis was performed using the vendor-supplied software.

2.3.4 Effect of VOC Contamination on the Wettability of Gd_2O_3 and Dy_2O_3

The wettability of Gd_2O_3 and Dy_2O_3 surfaces was studied as a function of their surface chemistry. For these experiments, we oxidized a metal foil to produce the corresponding metal oxide substrate. We note that unlike Al_2O_3, the oxides of Gd and Dy do not provide long term protection for the underlying metal from reacting with water. *However, during the course of the WCA measurement, which only lasts several to several tens of seconds, we did not observe any reaction between water and the substrate.*

The WCA of an as-received Gd foil, which is covered by a native Gd_2O_3 layer, was 97^o (Figure 7a). To remove any possible adsorbed hydrocarbons on the surface, Gd foils were annealed in air at 1050^{o}C for 40 minutes (with 20 min ramp); in addition to removing the adsorbed hydrocarbon, the high temperature treatment also oxidized additional Gd to Gd_2O_3. Immediately after the annealing, the sample exhibited super-hydrophilic behavior, giving a WCA of 0^o (Figure 7a, measured within 2 min of annealing treatment). However, upon exposure to ambient air, the WCA gradually increased over time and plateaued at *ca.* 84° after 10 hours (Figure 7a-b). Similar

change of wettability was also observed on Dy_2O_3 samples: a Dy_2O_3 surface showed 0° WCA immediately after annealing at 1050°C and the WCA increased to 66° after 12 hours of exposure to ambient air. To verify that it is airborne hydrocarbon that is responsible for the observed wetting transition, 1-octadecene ($C_{18}H_{36}$, ODE) vapor was introduced to a freshly annealed Gd_2O_3 sample. The time evolution of the WCA increase was drastically accelerated (Figure 7b inset).

The surface contamination by airborne hydrocarbons was further verified by XPS. For these experiments, a Dy foil was annealed in air at 1050°C for 1 hour to form a thin layer of Dy_2O_3. Upon removal from the annealing chamber, the foil was transferred to an XPS instrument as described above. Figure 4c shows the C1s and Dy4p3 region of the XPS spectra. As can be seen, the carbon peak increased after exposure to ambient air. The C : Dy atomic ratio was 1: 32 in the freshly annealed sample and increased to 1 : 8.9 after exposing to air for 2 months. To verify that the carbon peak was indeed due to the adsorbed hydrocarbon on the surface, the surface was sputtered with Ar^+ ions; we observed an immediate disappearance of the C1s XPS peak (Figure 7c).

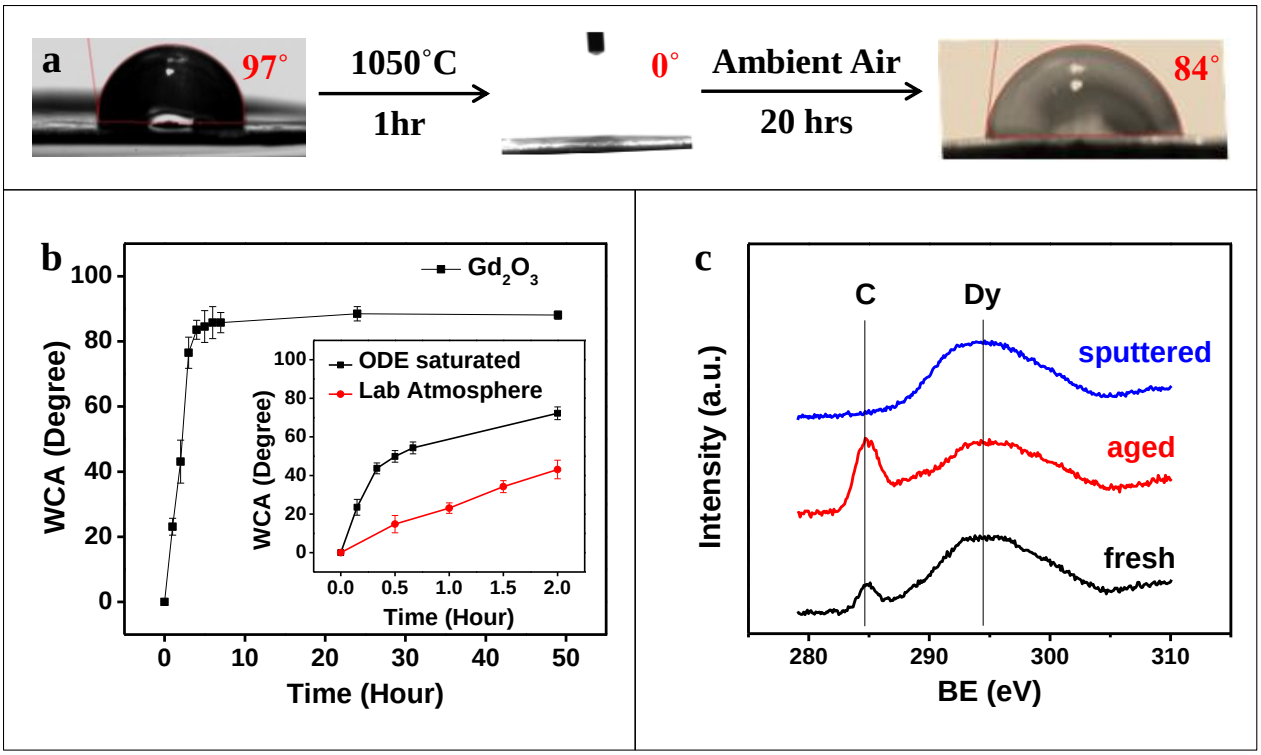

Figure 7. a. Effect of thermal annealing and air exposure on the wettability of a Gd_2O_3 substrate. **b.** WCA of Gd_2O_3 substrate as a function of air exposure time. The inset shows the effect of ODE vapor on the time evolution of the WCA. **c.** XPS spectra of fresh, aged (2 months), and Ar^+ ion sputtered Dy_2O_3 substrate.

2.4 Effect of Hydrocarbon Contamination on the Wettability of CeO_2

We have studied the correlation between surface cleanness and wettability of CeO_2. The CeO_2 sample was donated by Varanasi lab; it was deposited by sputtering on a silicon wafer and stored in air for several weeks prior to our analysis. When received, the sample gave a WCA of 98.7º and XPS (Al-Kα, hν=1486.6eV) analysis showed that there was relative atomic ratio of 21.9% Carbon on the surface. Similar high carbon content was also found when analyzing CeO_2 and Dy_2O_3 samples prepared by oxidation of metal foils and air aging. We note that the XPS measurement only sets a lower bound of the hydrocarbon contamination because certain adsorbed hydrocarbons may desorb in high vacuum. Overall, these results indicate that REO surfaces are capable of adsorbing significant amount of hydrocarbon from air.

To obtain a hydrocarbon-free CeO_2 surface, we thermally annealed the sample to oxidize the adsorbed contaminants. We found that annealing the sample at 300 ºC resulted in incomplete removal of hydrocarbon while annealing at 800 ºC produced crack lines in the sample (Figure 8). For the sample annealed at 500 ºC for 45 minutes, no crack or damage was observed by optical microscopy and AFM. For this sample, a carbon content of 4.75% was measured by XPS and the WCA data measured immediately after the annealing was 0º (Table 1 #2; Figure 8). After stored in ambient for 24 hours, its carbon content increased to 9.82% and WCA increased 56.3º; after 2 weeks, the carbon content and WCA ultimately reached 12.9% and 65.6º, respectively (Table 1 #3-4; Figure 8). This result shows that the CeO_2 surface is hydrophilic after removing hydrocarbon contaminants; re-adsorption of hydrocarbon from air results in an increase of its hydrophobicity. Similar observations were also made using Gd_2O_3 and Dy_2O_3 samples prepared by annealing the corresponding metal foils in air (See SI for details).

Because thermal annealing could introduce stress on surface, we also evaluated the effect of surface relaxation on the wettability. In this experiment, a sputtered CeO_2 sample was thermally annealed (500 ^oC, 45 min) and then stored in an ultra-high vacuum (UHV) chamber ($7x10^{-10}$ Torr) for 24 hours to relax the surface. The surface carbon content increased slightly (from 4.75% to 7.01%) during the UHV aging, likely due to the adsorption of residual hydrocarbon in the UHV chamber (Table 1 #5; Figure 8). The WCA measured immediately after the UHV aging was 33.1^o. Further storage in ambient air resulted in an additional increase in the WCA, reaching 65.8^o after 2 weeks (Table 1 #6; Figure 8). This data shows that surface relaxation, if any, does not significantly impact the wettability of CeO_2.

Table 1. WCA and surface carbon content of CeO_2 samples

Sample #	Treatment Conditions	WCA (˚)	% Carbon
1	**As received CeO_2 thin film on Si wafer**	**98.7**	**21.9**
2	**Thermal annealed CeO_2 samples at 500 ^oC**	**0**	**4.75**
3	Sample 2, aged in air for 24 hr	56.3	9.82
4	Sample 3 after an additional aging in air for 2 weeks	65.6	12.9
5	Sample 2, aged in UHV for 24 hr	33.1	7.01
6	Sample 5 after an additional aging in air for 2 weeks	65.8	12.8

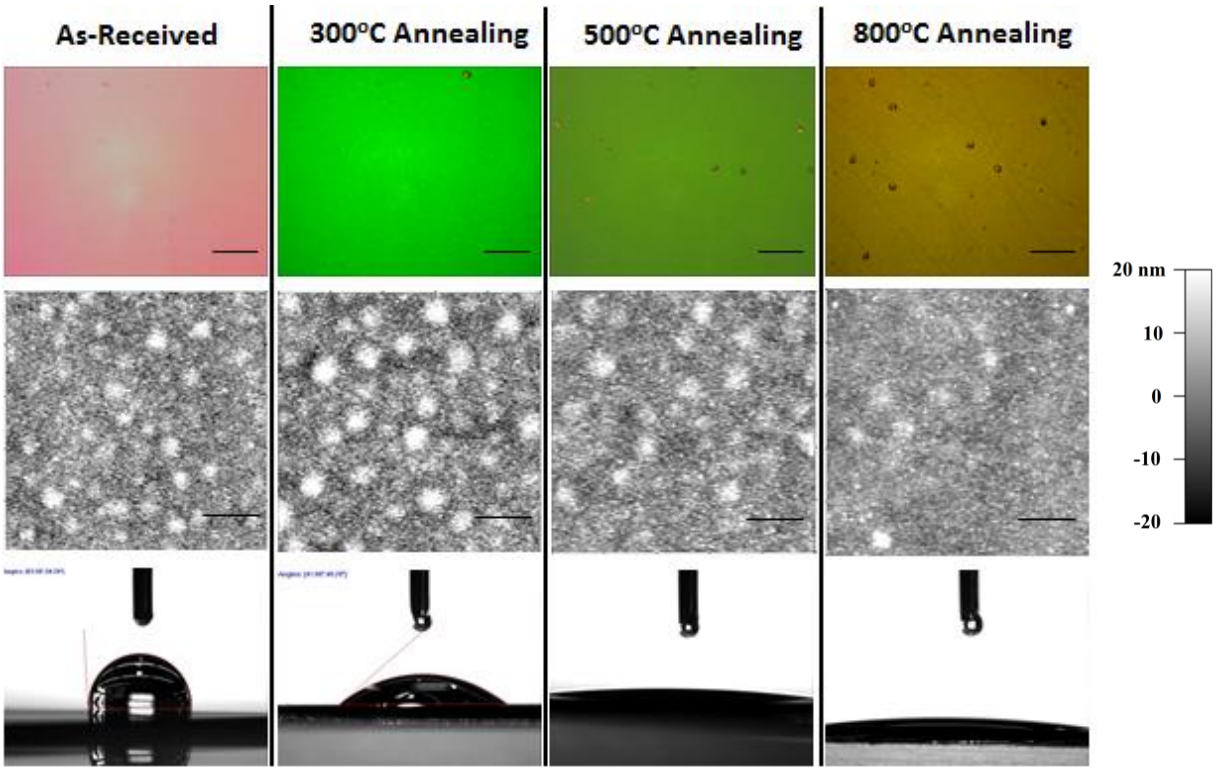

Figure 8. Optical micrograph (top; scale bar: 50 μm), AFM (middle; scale bar: 2 μm), and WCA measurements of CeO_2 samples. Surface cracks in CeO_2 film were only observed in sample annealed at 800 ºC. The difference in the color is due to variation in the thickness of CeO_2 and changes in the underlying silicon; pink to green color variations were seen on the as received, untreated sample.

2.5 Additional Evidence of Gydrocarbon Contamination in Azimi *et al.*

We note that Azimi *et al.* also conducted thermal annealing experiments; however, they observed that the hydrophobicity of REO was *maintained* after such treatment.[53] For example, the authors coated CeO_2 film onto silicon microposts and after annealing in air at 500 ^oC for 2 hours, they observed significant damage on the CeO_2 film. Despite such damage, a WCA of 125^o was observed by Azimi *et al.*, in stark contrast to the 0^o value reported here. We believe that the difference in the results again suggests that the samples used by Azimi *et al.* were contaminated by airborne hydrocarbon. In our work, hydrocarbon contamination was minimized by measuring WCA *immediately* after the annealing treatment.

Additionally, immediately after the initial submission of this comment, Varanasi lab reported another study in which showed that a freshly prepared CeO_2 sample is hydrophilic (WCA = 15^o).[68] They also observed *ca.* 12% of carbon contamination on a CeO_2 sample that has been stored in a vacuum desiccator; this sample gave a WCA value of 104^o. However, the authors attributed the hydrophilic behavior to high surface O/Ce ratio (~ 3.0) and the hydrophobic behavior to close to stoichiometric O/Ce ratio (~2.2). In contrast, in our work, hydrophilic behavior was observed even on samples with O/Ce ratios close to ~2.2. For example, the thermally annealed sample (Appendix A1b) gave an O/Ce ratio of 2.1 and a WCA of 0^o. For the sample that was thermally cleaned and 24 hr UHV aged, an O/Ce ratio of 2.3 and 7.0% of carbon was observed (Appendix A1c); this sample gave a WCA of 33^o. The positive correlation between surface contamination and WCA is exemplified in Figure 6**.**

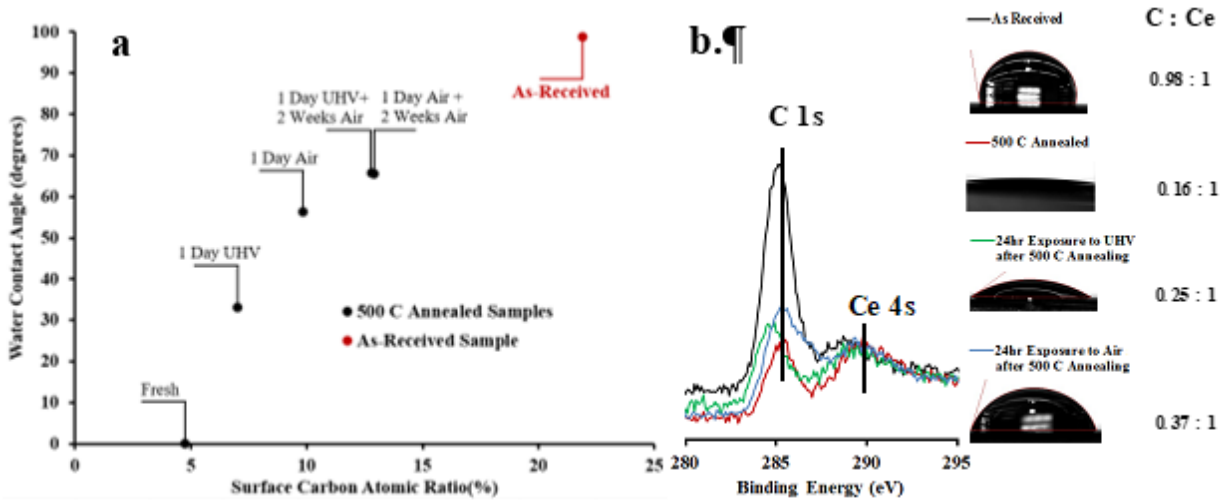

Figure 9 Correlation between surface contamination and WCA a. Time evolution of WCA of a CeO_2 sample after thermal annealing. The sample was exposed to ambient air either immediately after the annealing (black) or after annealing and storage in UHV for 24 hr (red). b. C1s and Ce4s XPS peaks of CeO_2 samples: as received (black), thermally annealed (red), annealed and aged in UHV (green), annealed and aged in air (blue). The right column shows the WCA data and Carbon : Cerium ratios measured by XPS.

2.6 Conclusions

In summary, our data as well as recent data from Varanasi lab strongly suggest that the REO samples used in Azimi *et al*. were unintentionally contaminated by airborne hydrocarbon. This contamination casts doubt on their claim that REOs are intrinsically hydrophobic because such hydrophobicity could be attributed to the adsorbed hydrocarbon. Our data further confirms that REOs are indeed intrinsically hydrophilic and become hydrophobic due to the adsorption of airborne hydrocarbons. Since the initial revision of this work in 2014, other independent reports had also arrived to similar conclusions as ours, and challenged the findings of Azimi *et al.*[54-59] Collectively, these evidences suggests that the performance of REO-based hydrophobic coatings will depend on the presence of hydrocarbons in the environment and may be negatively impacted if the adsorbed hydrocarbons are removed by thermal or oxidative (*e.g.*, UV/O_3) processes.

3.0 Dynamics of Airborne Contamination of Graphite as Analyzed by Ultra-Violet Photoelectron Spectroscopy

3.1 Chapter Preface

Sections of the material in this section was part of a research article published in the *Journal of Electron Spectroscopy and Related Phenomena.*

List of Authors: Muhammad Salim, Justin Hurst, Michelle Montgomery, Nathan Tolman, Haitao Liu

Author Contributions: M.S. and H.L. designed and directed experiments. M.S., J.H., M.M., and N.T. conducted the experiments. All authors discussed the results and M.S. and H.L. co-wrote the manuscript with input from authors.

3.2 Introduction

Until recently, graphitic carbons, such as HOPG had been considered intrinsically hydrophobic surfaces. However, Li *et al.* showed that a freshly exfoliated HOPG surface increases in hydrophobicity after exposure to ambient air for only a few minutes. This phenomenon is due to the adsorption of airborne contaminants. The time-dependence of the surface contamination processes have been studied and reported previously.[2, 69-70] These adsorbed molecules are primarily VOCs and form a surface contamination layer—the thickness of which evolves over time, increasing and plateauing to about 0.55 nm within an hour of air exposure, for HOPG.[2, 69] Beyond HOPG, studies have also shown similar surface contamination to occur on a wide range of surfaces (*e.g.*, Au, TiO_2, SiO_2, and graphene)—resulting in a universal increase of their WCA.[21-22, 69]

A hydrocarbon-contaminant-free graphite surface behaves very differently from that of contaminated ones. It is of great interest to fully characterize the coverage and chemical nature of the surface contamination on graphite, especially since composition influences surface behavior.[2, 40, 71-74] For example, the heterogeneous electron transfer rate from HOPG to solution redox couples increases by at least 2-3 orders of magnitude when the surface was made clean.[40] The double layer capacitance of graphite could decrease by up to 70% upon airborne contamination.[38] Surface cleanness also impacts interfacial chemical processes, such as atomic layer deposition (ALD) of metal oxide on graphene/graphitic surfaces. In these processes, the nucleation event is sensitive to polar structures, such as defects and step edges of graphite as well as polar functional groups of adsorbed contaminants from ambient.[75-76] These results are consistent with the expectation that even a monolayer amount of contaminants should impact surface sensitive properties.

There have been many efforts to characterize the airborne-hydrocarbon contaminations on graphitic substrates. For example, Kelvin probe force microscopy (KPFM) was used to study

adsorption of polyaromatic hydrocarbons on graphite in a vacuum chamber.[77] High resolution AFM has recently shown the presence of well-ordered airborne contaminants on graphite stored in ambient conditions.[78] We and others have also used XPS, Fourier-transform infrared spectroscopy (FTIR), and ellipsometry to study the intentional adsorption of organics as well as unintentional airborne and waterborne contamination of graphene and graphite.[2,11, 38, 71, 79-80].

Despite these progresses, there is still very limited understanding of the chemistry of the contaminants, especially at the early stages of contamination. For example, the main challenge for characterization by XPS is the extensive overlap in the C1s spectral region of carbon in different chemical bonding states, making traditional peak fitting extremely challenging for detecting adventitious carbon contamination on carbon surfaces. FTIR can provide significant chemical information but suffers from poor time resolution and low sensitivity at low surface coverage. In addition, due to the conductive nature of HOPG, the surface selection rule makes it challenging to detect the IR modes that have their dipoles parallel to the surface. SIMS provides rich chemical information but is difficult to quantify. Neither ellipsometry nor KPFM provides chemical identity of the surface contaminant. Lastly, measurement of contamination coverage and thickness by AFM suffers from poor time resolution and may be unable to detect contamination height changes, presumably due to mobility of the contaminants on the surface (see supplementary information Figure S1-S4).

In this paper, we study the time evolution of the surface contamination of HOPG by using ultra-violet photoelectron spectroscopy (UPS). UPS is closely related to XPS, which has been extensively used in the analysis of surface contaminations, including those on carbon surface we and other reported recently.[2, 11, 37] Here, we present UPS as a surface sensitive characterization technique that offers key advantages over XPS.

First, UPS provides much richer information on the chemical bonding than XPS does. UPS probes valence electronic states by utilizing UV photons typically of less than 50 eV in energy, whereas XPS utilizes soft X-ray photon sources Mg Kα (1254 eV) and Al Kα (1487 eV) to probe core-level electronic states.[81-82] In this sense, XPS and UPS are complementary in studying molecular adsorption onto solids. Incidentally, the cross section for photoelectric excitation of the outer-shell electrons for the second-row elements is much smaller for XPS than UPS. At 21.2 eV (He I), the C2p cross section is over ten times that of C2s cross section, while at 1400 eV, the C2s cross section is over ten times larger than the C2p cross section. Thus, at UPS photon energies, the C2p states are greatly emphasized over the C2s derived states. This property makes UPS a much more sensitive tool than XPS to probe the valence states, molecular bonding and chemical composition information of surface adsorbed species, and allows UPS to clearly differentiate between carbons in different chemical states.[82-84]

Second, UPS provides much higher surface sensitivity than XPS. For all photoelectron spectroscopy (PES), the inelastic mean free path, λ, of the photoelectrons are substrate and energy dependent. The sampling depth of PES is usually taken as 3λ. This depth accounts for 95% of the photoelectrons at normal takeoff angle, of which 63.3% is from 1λ depth. The sampling depth of 1487 eV photon (Al Kα used in XPS) in graphite is 8.7 nm, or 26 layers of graphene. At 40 eV (He II line used in UPS), the sampling depth becomes 1.71 nm, or about 5 layers of graphene.[85-86] Note that since PES is also substrate dependent, adsorption of a contamination layer will change the sampling depth - a decrease of surface density would result in an increase of the mean free path.[86-87] These characteristics of UPS enables an enhancement of signal from the top organic contamination layer adsorbed on substrates compared to the case of using XPS. A simple representation of this is shown in Figure 10. Due to the carbon-rich nature of the HOPG substrate

and of the organic contamination, UPS is an attractive option for analysis of carbon substrates because it highlights the photoelectron signal from the top thin contamination layer rather than the bulk of the substrate.

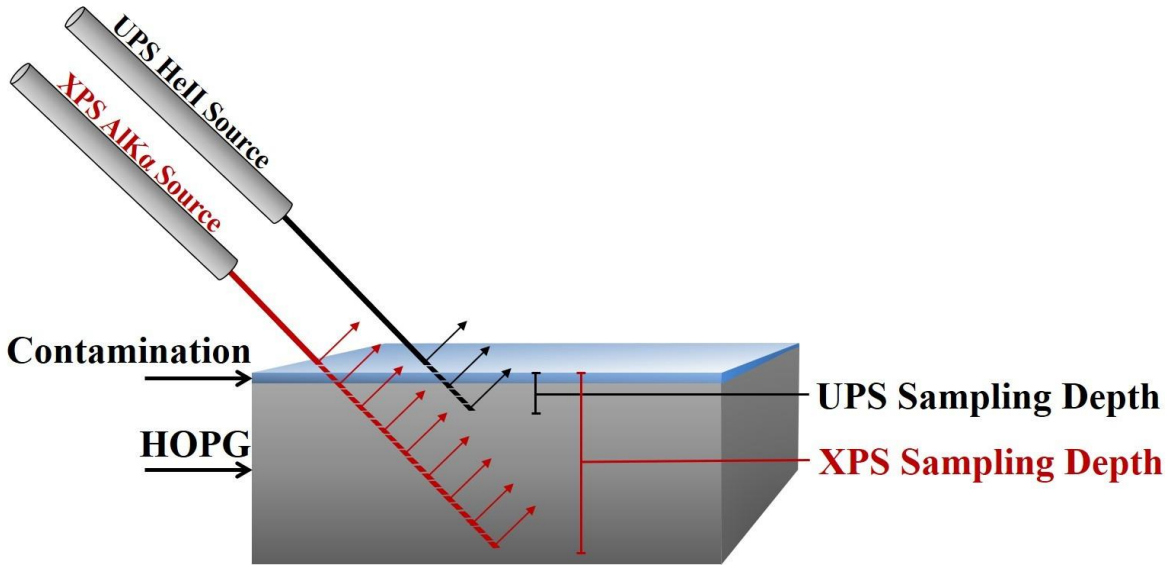

Figure 10. Illustration of relative sampling depth analyis for UPS and XPS on graphitic carbon.

3.3 Materials and Methods

3.3.1 Photoelectron Spectroscopy

UV photons (He II 40.8 eV) generated at a power of 0.4W (0.58mA; 0.68kV) in a differentially pumped gas discharge lamp (He 0.025mBar) in an ESCALAB 250Xi photoelectron spectrometer. Photoelectrons were analyzed at pass energy 10eV, with a Spot size of 0.4mm and take-off angle of 45°. Correlated XPS measurements were taken immediately following each UPS measurement. XPS measurements were performed using monochromatic Al Kα X-rays (hν=1486.6 eV) generated at a power of 145 W (10 mA; 14.5 kV). Spot size was 0.4 mm with a take-off angle of 45°. High resolution XPS data were gathered by using a minimum of 40 scans for O1s and 7 scans for C1s with a pass energy of 50eV. Since the sample being analyzed is conductive, no charge neutralization was used. Cleaving of HOPG (SPI Supplies SPI-2 Grade) in UHV was performed at $4x10^{-7}$ mBar in the preparation chamber of the instrument. Exfoliated samples were directly transferred into the UHV analysis chamber with pressures around $8x10^{-10}$ mBar. UPS measurements were taken within 5 minutes of exposure to UHV for samples cleaved in the preparation chamber, and within 20 minutes for air-aged samples. The temperature and relative humidity for experiments conducted in air was 22.4 ± 2.4°C, and 26.6 ± 3.8% respectively. Due to operation requirements of the He II source, pressures in the analysis chamber increased to a range of $5x10^{-8}$ to $8x10^{-7}$ mBar. Thermo Scientific™ Avantage™ software was used for data collection and peak analysis.

UHV cleavage was performed by first attaching UHV copper tape to the surface of a HOPG sample and anchoring the other end of the tape within the preparation chamber. During transfer of the HOPG sample from the preparation to analysis chamber, the lateral movement of the sample

removes the UHV tape from the surface of the HOPG—thus cleaving the HOPG, resulting in a pristine surface with full and complete removal of the top HOPG layer. A schematic of this setup is shown in Figure 11.

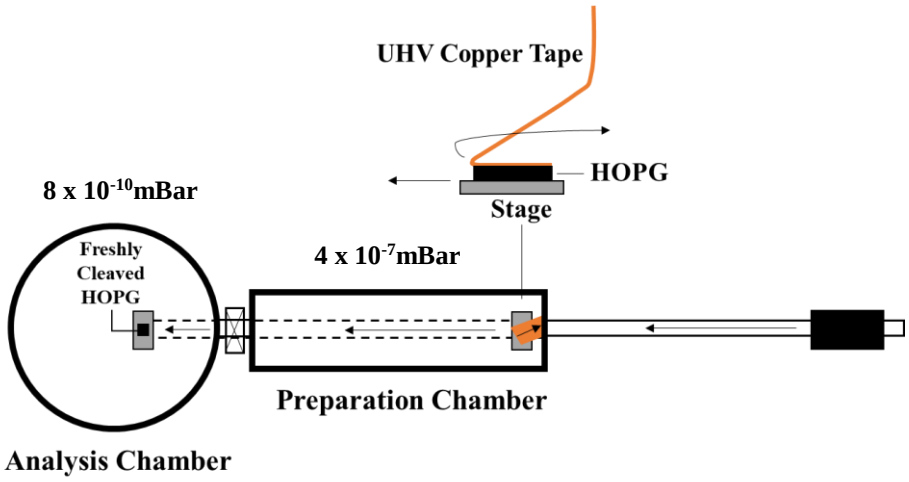

Figure 11. UHV cleavage of HOPG. HOPG is exfoliated during transfer into the analysis chamber of the ESCALAB 250Xi spectrometer.

3.3.2 Water Contact Angle

WCA measurements were collected with a VCA Optima XE contact angle system. Each water droplet had a volume of 1 μL and was carefully touched to the sample surface. A charge-coupled device (CCD) camera was used to take images of the water droplets. Each WCA mesurement was repeated 6 times. The first measurement was conducted within 5s of air exfoliation.

3.3.3 Ellipsometry

Thin film thickness was determined by spectroscopic ellipsometry (SE). A J. A. Woollam Alpha-SE spectroscopic ellipsometer recorded data between the wavelengths 381 and 893 nm, at an incident angle of 70°. The first measurement was conducted as the HOPG was exfoliated.

3.3.4 ATR-FTIR

FTIR spectroscopic measurements were taken using a germanium tip in attenuated total reflectance (ATR) mode on a Bruker VERTEX-70LS FTIR and a Bruker Hyperion 2000 FTIR microscope. Measurements were taken from 600 to 4000 cm^{-1} with a resolution of 4 cm^{-1}. The ATR tip was swabbed with isopropyl alcohol prior to measurements. At least 5 min was allowed for the isopropyl alcohol to evaporate before measurements were taken. HOPG was characterized by ATR-FTIR after being exposed to air. The sample was exfoliated, and the first measurement was conducted within 30 s.

3.4 Results and Discussions

Exfoliation of HOPG produces a clean surface, which readily adsorbs VOCs upon contact with ambient air. We will first discuss characterization results from atomic force microscopy (AFM), WCA, Ellipsometry, and ATR-FTIR. We will then discuss the XPS and UPS results in detail; advantages of UPS over XPS for detection of carbon species on a carbon substrate will be highlighted.

3.4.1 Contamination Layer Characterization by WCA, ATR-FTIR, Ellipsometry, and AFM

We imaged the HOPG surface with tapping mode AFM, both immediately following its exfoliation (< 1 min) and after controlled amount of air exposure (2 hour, 24 hour). The AFM images (Appendix B1 – B4) show the typical morphologies expected for HOPG. However, no noticeable changes were observed between the images. It is likely that the adsorbed VOCs are too mobile to be detected by AFM.

WCA provides a qualitatively assessment of the changing chemical composition on a surface. In this study, an initial WCA was measured to be 59^{o} immediately after exfoliation of HOPG, increasing to 69^{o} after 5 minutes, and 89^{o} after 15 minutes of air exposure. For longer air exposures the WCA was measured to be 91^{o} after 2 hours, and 98^{o} after 24 hours. This data (Figure 12a) is very similar to our previous reports.[38, 74]

Although a large increase of WCA from 59^{o} to 89^{o} occurs within the first 15 minutes, only minute changes were observed in longer exposures. Indicated by the initial high rate of change and eventual plateauing of WCA, contamination accumulation in the early stages contains the

important and largest relative composition changes for WCAs observed in longer air exposures. The small change in the long term, however, does not necessarily imply a small change in the composition of the contamination layer. This is because WCA measurement cannot detect composition changes that do not alter the wettability.

For further representation of the changing surface chemistry of HOPG exposed to air, ATR-FTIR (Figure 12) measurements were collected. ATR-FTIR was performed within 30s after exfoliation (Fresh) and after longer air exposures (10 min, 20 min, 30 min). A general trend of increasing symmetric and asymmetric C-H stretches were observed as air exposure time was increased; an increase in C-H peak corresponds to an increase of adsorbed volatile carbon content (VOCs) on the surface. However, the rate of peak intensity increase would vary between samples, due to differences in separate exfoliations and in the air composition (*e.g.*, VOC concentration and relative humidity). This trend has been previously reported.[38]

The accumulation of VOC is also observed by ellipsometry (Figure 12c), with an initial large growth in VOC contamination film thickness—reaching 0.15 nm within 15 minutes, 0.50 nm after 2 hours, and plateauing off around 0.55 nm at 3 hours and up to *ca.* 16 hours. The increase in VOC content and contamination thickness, shown by ATR-FTIR and Ellipsometry, is correlated to the trends we see in WCA. In all three cases, changes occur rapidly after exfoliation but levels off after *ca*. 1 – 2 hours.

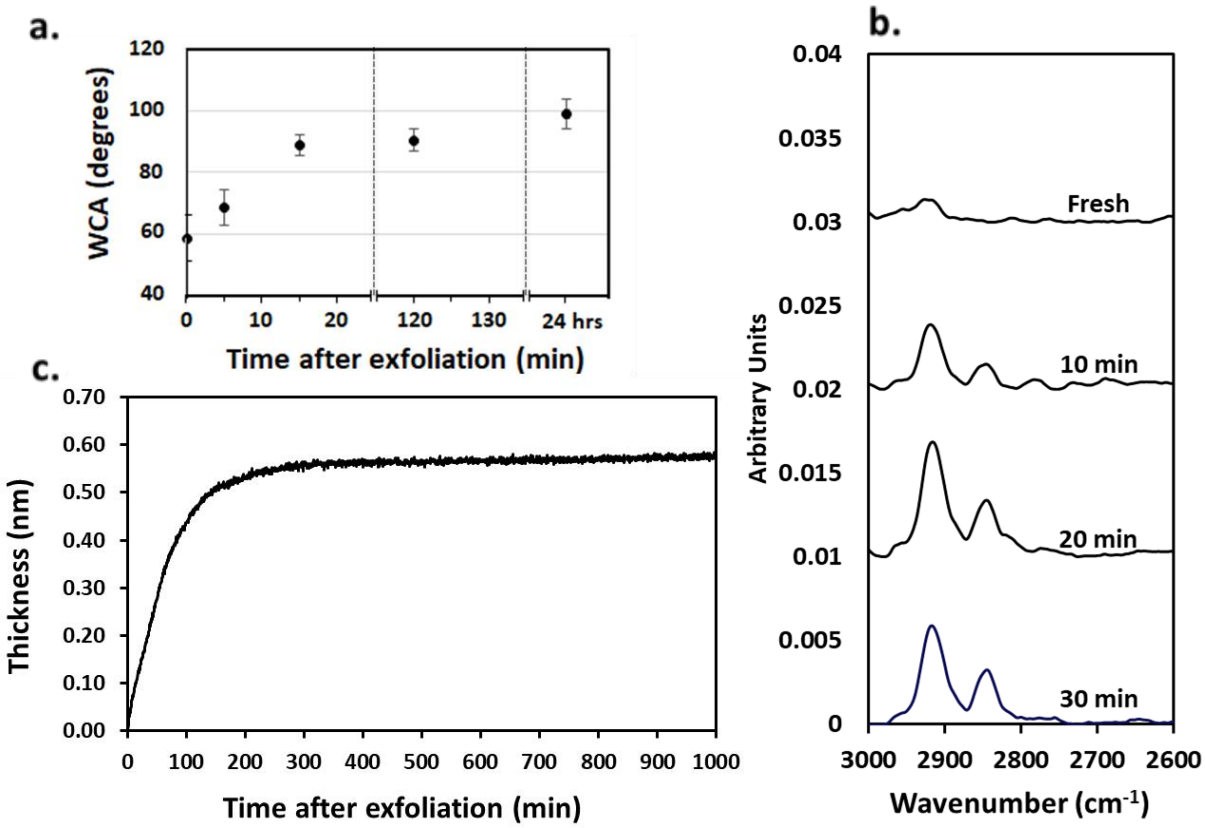

Figure 12. a. WCA of exfoliated HOPG at increasing air exposure times. Due to limitations of the technique, 0 min corresponds to 5s of air exposure. b. ATR-FTIR of C-H region for exfoliated HOPG at different air exposure times. Due to limitations of the technique, the *Fresh* measurement is taken after 30s of air exposure. c. Continuous Ellipsometry measurement of exfoliated HOPG exposed to ambient air, from time of exfoliation to 1000min. The first measurement was taken during exfoliation.

3.4.2 XPS

XPS has been used to characterize adventitious carbon adsorbed on graphitic carbon and other substrates. In this study, XPS data were collected alongside UPS measurement and such data should provide quantitative elemental composition of the surface. The XPS measurements provided in Figure 13a show the C1s and O1s data for various air exposure times. Due to the large escape depth (8.7 nm) of XPS photoelectrons in HOPG, much of the signal in the carbon XPS measurements originate from bulk HOPG, as mentioned earlier. This limitation makes it difficult to discern the XPS chemical information origination from the top thin contamination layer from that in the bulk of the sample, since both materials are carbon based. Additionally, this limitation is further complicated by the high degree overlap of XPS peaks of various types of carbon species (*e.g.*, C-OH vs C=O). As such, no change in FWHM of the C1s peak was observed from freshly exfoliated to 20 hr air exposure, as is shown in the insert of Figure 13a. Additionally, we observed no reduction in the shake-up satellites of graphite at 291eV. This XPS C1s data seems to suggest that there is no change in the surface carbon composition on graphite from freshly exfoliated to aged 20 hr in air. However, we know this to be incorrect, given that our data collected by ATR-FTIR and Ellipsometry clearly shows growth of an adventitious carbon layer that changes the hydrophobicity of the surface, so a composition change is present.

The XPS O1s peak also provides limited information for analyzing the early stage of the contamination dynamics. As shown in Figure 13b, the O1s signal is very low for samples with up to 20 hr of air exposure. This low signal makes it impossible to deconvolute the O1s peak for the purposes of chemical characterization. As will be shown below, for the same air exposure, the UPS spectra will show a significant change from the UHV-exfoliated one (Figure 14) at oxygen containing regions.

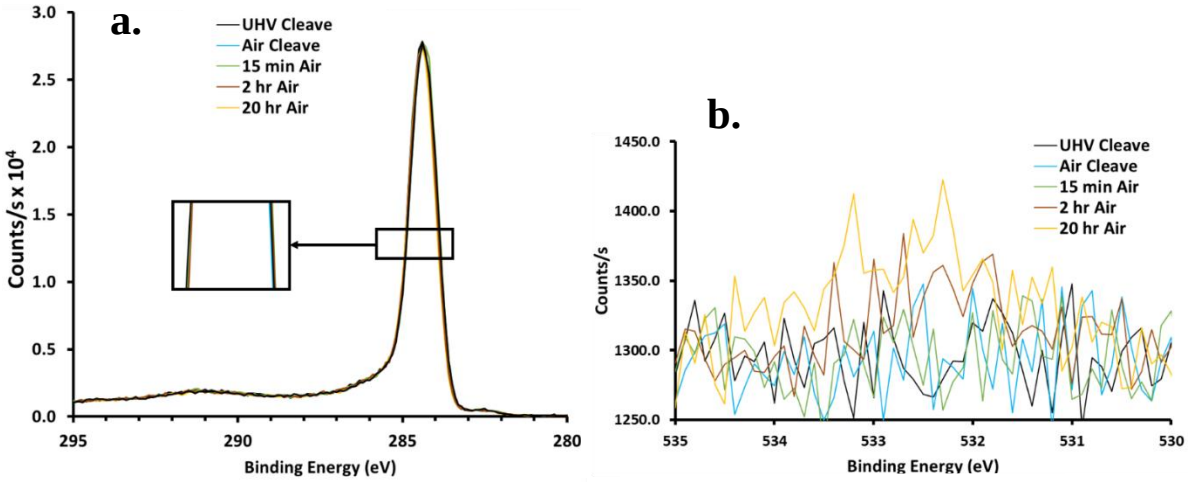

Figure 13. a. High resolution C1s XPS spectra of Air cleaved, Air aged, and UHV cleaved HOPG. Spectra are normalized to highest peak. The inset shows the magnified view of the FWHM region. **b.** High resolution O1s XPS spectra of HOPG samples.

In summary, our data shows that XPS is unable to differentiate between contamination and graphitic carbon and hence offers limited insight into the dynamics of the contamination layer on HOPG.

3.4.3 Characterization of Adventitious Carbon Contaminants by UPS

In order to facilitate analysis of the UPS data, we briefly review related UPS studies below, with consolidated data in Table 2 and 3. UPS has been used for the characterization of both organic thin films and of molecular adsorption on surfaces. Extensive studies with sputtering and film growth of different amorphous systems, graphitic systems, HOPG, and polymers have shown the changing convolution of density of states (DOS) correlating to surface composition.[88-93] Studies involving deposition and H-plasma treatment of a styrene film exemplifies the sensitivity of UPS, where sputtering results in a shift towards a UPS spectrum similar to a:C or a:C-H.[92, 94] UPS has also been used to verify the reduction of oxygen chemisorbed on graphene.[95] Other experiments have studied molecular adsorption of water or organics on metal surfaces, where UPS was used to study and characterize the dynamics of surfaces.[96-104] Although comparisons of adsorbates on other substrates provides insightful and useful information, it is not a perfect comparison to HOPG. In some cases, the existence of an interfacial dipole between HOPG and adsorbed molecules could also lead to a small (0 to 0.5 eV) shift in the binding energy, as was observed with hexobenzocoronene (HBC) adsorption on Si wafer or HOPG.[105] There are also extensive UPS studies on amorphous carbon (a-C) and hydrogenated amorphous carbon (a-C:H) films.[88-91, 93, 106-107] Typical a-C films consist of primarily sp^3 and sp^2 carbon clusters, with hydrogen contents ranging from 20%-50% having been prepared for a-C:H films. Structure amorphous carbons are characterized as localized clusters, ranging from diamond (sp^3) and polymer (sp^2 and sp^3 mixture)

like clusters to that of graphitic (sp^2) clusters.[87, 106, 108] The π states lie closer to the Fermi level and tend to form both the valence and conduction band edges. The minimum gap is always a π to π* transition.[88, 90] A large FWHM for peaks in the He II spectra for a-C and a-C:H, as well as for hydrogen and argon sputtered carbon surfaces, is attributed to the large distribution of various carbon-containing molecules present in the amorphous carbon films or the resulting sputtered surface. This extensive distribution of molecules provides an array of varying local π and σ states, resulting in a DOS summation that is a convolution of the DOS from each contributing molecule.[89]

Table 2. UPS He II peak binding energies relative to the Fermi level (E_f) for the characterization of adsorbed molecules on various substrates

Target Molecule	*Substrate*	*BE(eV)*
H_2O	Ni (Cond.)	6.5, 9.2, 13.0[109]
	Au (Cond.)	6.3, 10.2, 12.6[109]
	NpO_2	10.7[97]
	TiO_2	7.8, 9.8, 13.2[99]
	*Thin Film	7.1, 9.3, 13.2[101]
O-H	Ag	9.8, 12.5[110]
CO_2	Ag(111)	6.7,11.1, 12.7[111]
	Ni	7.4, 11.4, 12.9[109]
	Au	6.8, 9.3, 11.0, 12.5[109]
CO	Ni	6.3, 8.1, 11.1[109]
	Ni(100)	7.5, 8.1, 11.1[112]
	Pd(111)	7.3, 8.2, 11.0[113]
Methanol	Fe	6.1, 7.6, 10.1, 11.1, 12.4[103]
	Ni	5.8, 7.0, 9.8, 12.3[103]
	Cu	6.5, 8.1, 10.6, 12.8[103]
Diethylether	Fe	6.2, 8.1, 8.8, 9.9, 12.0, 14.5[103]
	Ni	4.8, 7.5, 10.2, 11.7, 15.3[103]
	Cu	5.6, 7.7, 10.4, 12.3, 15.9[103]
Acetalaldehyde	Fe	5.5, 8.0, 10.5[103]
Acetone	Ni	4.6, 8.5, 10.2, 12.65[103]
	Cu	5.5, 9.1, 11.2, 13.7[103]
Methylacetate	Fe	6.4, 8.4, 10.1, 12.0, 14.3[103]
	Ni	5.8, 7.7, 9.4, 11.35, 13.6[103]
	Cu	6.5, 8.5, 10.3, 12.2, 14.5[103]
Acetic Acid	*Thin Film	6.7, 8.9, 11.5[101]

*Denotes thin film of target molecule

Table 3. UPS He II peak assignment. Binding energies are relative to E_f of the substrates

Substrate	*Assignment*	*BE (eV)*
Graphite[96]	π	0.7
	π	3
	π, σ	5.7
	σ	8
	σ	13.6
a-C:H[92]	π	4 (broad)
	σ	7 (broad)
**Styrene Thin Film*	π	3.2
	Undefined	7.0, 8.7
a-C:H[89]	π	4
	σ	7.6
Graphite[89]	*Graphite*	13
**HBC 10nm films on:*[105]		
Si Wafer	π	1.6
	π	3.0
	mostly π, some σ	5
	increasing σ contribution	>5
	σ and π mix	3-8.8
HOPG	π	2.0
	π	3.5
	mostly π	5
Styrene[94]	π	3.82
	σ	6.37
	σ	8.62
H-implanted Graphite[91]	π	4
	σ	7.5
	σ	13
Graphite[114]	π	2.9
	σ	4.3
	σ	7.8
Graphite[115]	π	0-7
	σ	4-13.6
HOPG[116]	π	4
	σ	7
HOPG[117]	π	2.5
	π-σ overlap	5
	σ	8
	σ	13

*Denotes thin film of substrate

3.4.4 UPS Spectra of UHV- and Air-Exfoliated HOPG

UHV-exfoliated HOPG samples are presumed to be a pristine and uncontaminated surface—absent of VOC or other (*e.g.*, water) adsorbates. The UPS He II spectra from UHV-exfoliated HOPG correlates closely with previously reported spectra for *clean* graphite and HOPG.[91, 116, 118] Note that in our experiment, the HOPG sample is polycrystalline. As a result, the UPS spectra present here are very different from angle resolved UPS data collected from single crystal graphite.[114-115, 119] Instead, our UPS spectrum is a weighted convolution of the energy distribution curves at different polar angles—the largest contributors being from the flat, maxima, and saddle points in the band. UPS spectra of UHV-exfoliated HOPG (Figure 14) consists of a primary peak at 7.6 eV, with a shoulder peak at 5 eV, and a smaller peak at 2.9 eV. Referencing previously published UPS work on carbon substrates, these peaks are identified as originating from graphite σ, graphite π-σ overlap, and graphite π bands, respectively. A fourth peak, located at 13.7 eV, was previously observed for graphite, but not for a-C or a-C:H. [89, 96, 106]

We also conducted exfoliation of HOPG samples in air and measured their UPS spectra after varying amount of air exposure. Any contaminant adsorption on the surface is expected to change the total signal peak location/area, relative to the spectrum of UHV-exfoliated HOPG. Shown in Figure 7, these samples exhibit an immediate reduction in the intensity of the primary graphite σ peak at 7.6 eV relative to the total UPS spectral area. Gradual and increased broadening of this primary peak is also observed during increased air exposure. This broadening can be attributed to the increased amount and/or variety of adsorbed VOCs. Upon increased air exposure, the graphite π peak at 2.9 eV is observed to shift slightly downfield and increase in magnitude.

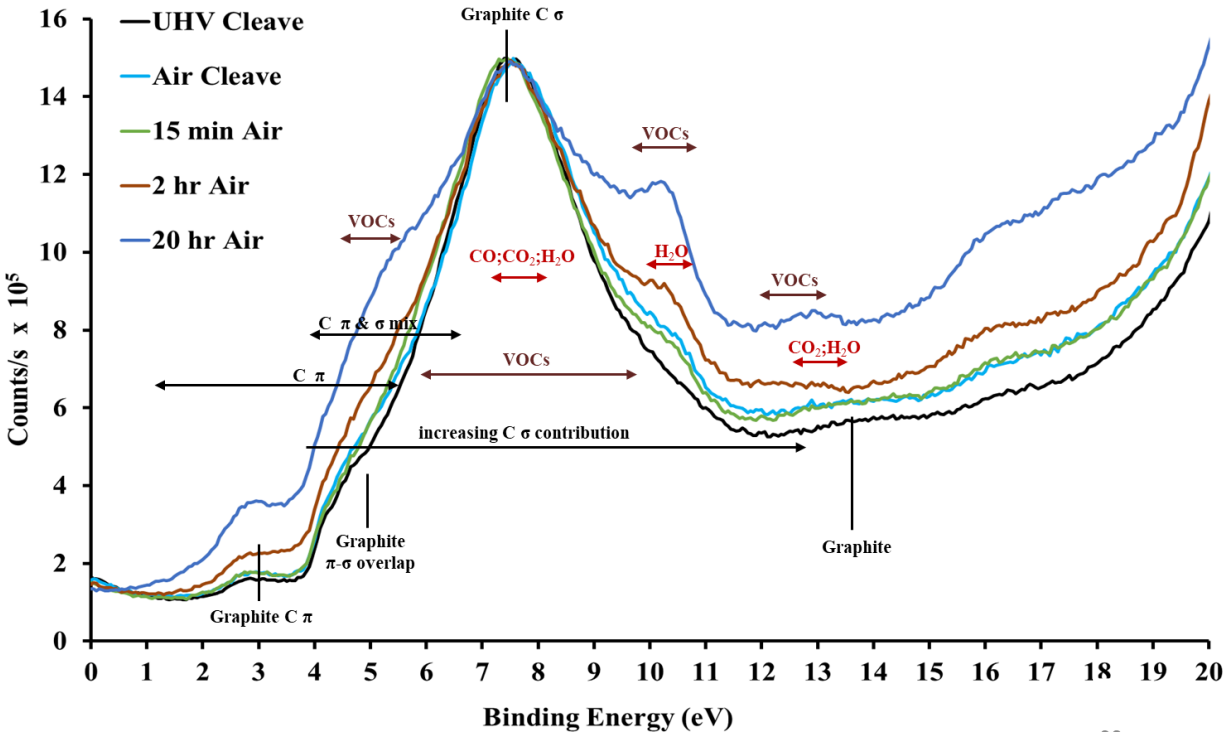

Figure 14. UPS spectra (He II, 10 eV pass energy) of HOPG after cleavage in UHV (UHV Cleave), after cleavage in air (Air Cleave) and exposing to air for varying periods of time (15 min Air, 2 hr Air, and 20 hr Air). Spectra intensities are normalized to the highest peak. Arrows denote binding energy regions that are from data in Table 2 and Table 3.

This shift phenomenon is also observed for the graphite peak at 13.7 eV—a gradual shift toward 12.8 eV is observed upon increasing air exposure, as well as a magnitude increase.

It is important to note that the UPS measurements were done in UHV and as a result, the UPS measurement underestimates the molecular adsorption under atmospheric pressure. Weakly bound species, likely low molecular weight and/or non-polar, could adsorb onto the surface under ambient conditions but desorb prior to the UPS measurement. Temperature programmed desorption (TPD) in UHV conditions of adsorbed organic molecules from graphene and graphitic surfaces have been reported and offer insight into what adsorbates may be present during UPS measurements. Small *n*-alkanes, like ethane or propane, have been show to desorb from graphene below 120 K in UHV.[120] An increase in *n*-alkane chain length results in a nonlinear increase of higher desorption energies.[121-123] Decomposition of longer alkanes, like *n*-octane, occurs at high temperature before desorption from graphitic surface.[124] Polar functional group, such as -COOH results in a net increase of adsorption energy. However, this enhancement is dampened as chain length is increased.[122] This improved adsorption of functionalized alkanes is attributed to the existence of functionalized surface sites on HOPG. As an example, the hydrophilic step edges of HOPG are known to strongly adsorb water vapors from air. Desorption of water bound to these defect sites have been shown to desorb at temperatures up to 235K. Adsorption of water ice multilayers on graphite is possible at very low temperatures, and desorption of such multilayers occurs between 140 and 170 K.[125,124] It has also been shown that chemisorption of O_2, CO_2, and H_2O occurs at room temperature on graphite, decomposing at temperatures between 450-1253K, depending on the chemical species. These adsorbed species were assigned quinone and lactone-like structures. Given that molecular species of H_2O, CO, and CO_2 physisorbed onto graphite will readily desorb below room temperature in UHV, any UPS peaks which align to these locations

represent either surface chemisorption, or respectively functionalized VOCs physisorbed to graphite.[126]

The chemisorption of O_2, CO_2, and H_2O on the defect sites of HOPG would also impact physisorption of small molecules. For example, the sticking probabilities of acetone on UHV annealed HOPG are more than a factor of two times smaller than on air cleaved HOPG, which contains functional groups.[127] Finally, we want to point out that although storage under UHV is usually considered as a method to maintain a clean surface, adsorption of contaminants in UHV could occur, as has been observed with KPFM studies of graphite samples stored in UHV.[77] We have conducted additional control to assess this possiblity in our studies. Figure 15 shows same-spot analysis of UHV cleaved HOPG at different times of UHV exposure. The *UHV Cleave* spectrum corresponds to 5 minutes of exposure in the UHV analysis chamber before measurement, and sequent measurements were performed on the same sample and same spot. There is almost no change in the spectrum for sample stored in UHV for 2 hours and even after 18 hours, only very minor changes were observed (See Figure 16 for differential spectrum). These results are in stark contrast to the air-cleaved data shown in Figure 11. We conclude that the background contaminaion from UHV chamber is neglible in our studies.

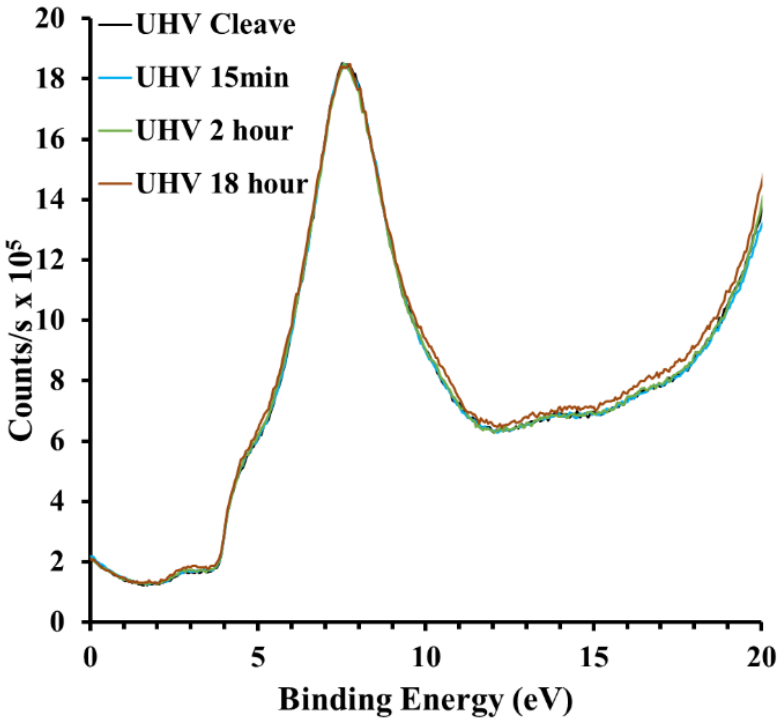

Figure 15. Same-spot UPS spectra (He II, 10 eV pass energy) of HOPG after cleavage in UHV (*UHV Cleave*) and after sequential exposures to the UHV environment of the analysis chamber.

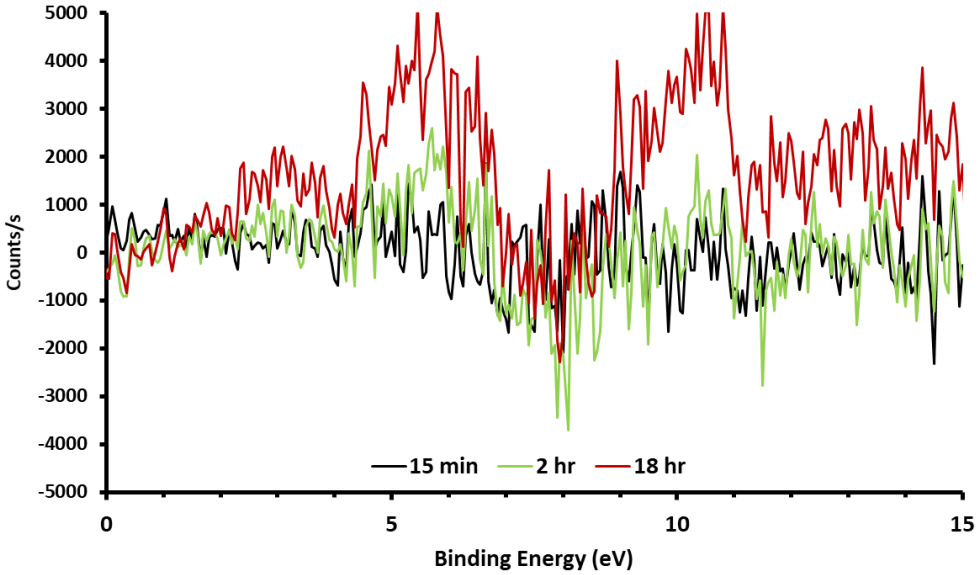

Figure 16. Difference spectra from Figure 12. Consecutive same-spot UHV exposure measurements were performed on HOPG cleaved in UHV. Each plot represents the difference spectra of UHV exposure time (15 min, 2 hr, 18 hr) UPS spectra subtracted by *UHV Cleave* UPS spectra.

3.4.5 Time Evolution of Hydrocarbon Contamination

The time evolution of the surface contamination can be qualitatively assessed based on the spectral evolution of the air-exposed samples. The kinetics of adsorption of VOCs onto HOPG have also been studied using attenuated total reflectance (ATR) measurements,[38] WCA measurement,[2, 71] and ellipsometry. [71] It is informative to compare the time evolution of the UPS measurement with these measurements.

Data presented in this work, as well as in previous work by us and others showed that very large WCA and Ellipsometry changes are observed for short term air exposures. However, there are only slight differences in the UPS spectra of 15 min air exposure and air cleaved samples in comparison to the UHV cleaved surface. Such similarity in the UPS data suggests that most of the initial adsorbates, although forming a substantial contamination layer that causes a significant increase of the surface wettability, readily desorb under UHV conditions. Therefore, most of the adsorbed molecules in short term air exposures are weakly bound, most likely lower molecular weight species. In addition, the existence of a small spectral differences between the air-cleaved sample and that of UHV-cleaved sample suggests that an immediate contamination occurs during the exfoliation of HOPG in air, which is not been possible to be detected by wetting, ellipsometry, or XPS measurements. We attribute this observation to the chemical functionalization of surface defect sites and/or adsorption of very strongly bound species to the defect sites, since more weakly bound species would be desorbed in UHV.

Notably, the UPS data provided in this study also supports a continued dynamic adsorption model of airborne contaminants, represented by the varying UPS spectra of long term air exposed samples, even after the WCA increase has halted (98^{o}) and the ellipsometry showed a plateau of adsorbate thickness (0.55 nm), typically within several hours.[71] In contrast, for the HOPG samples

with 2 hr and 20 hr air exposure, the UPS spectra showed a continues increase in the peak intensity near 5 eV and 10 eV, as well as an increase in the background, suggesting that higher molecular weight, more strongly adsorbed, molecules are present.

There is currently no detailed study on the chemical composition of the airborne contamination of HOPG. However, in related studies on other surfaces, the composition of the surface airborne contamination layer has been observed to change over time when exposed to multi-component gas mixtures—a result of dynamic competition of surface adsorption sites.[21-22] The adsorption-desorption competition and composition change of contamination has been studied for silicon wafers.[128-131] This selectivity driven molecular adsorption feedback loop with surface composition ultimately results a time-correlated fluctuation—from a freshly prepared and clean surface to an aged and contaminated surface. Silicon wafers have shown to exhibit such correlation and competition in bi- and multi-component gaseous mixtures. This phenomenon can be correlated with ambient air conditions, where the number of components in the contamination layer is greatly increased. [21-22] We expect similar complex behavior to be occurring on the HOPG surface we used in this study, as visualized by our UPS measurements.

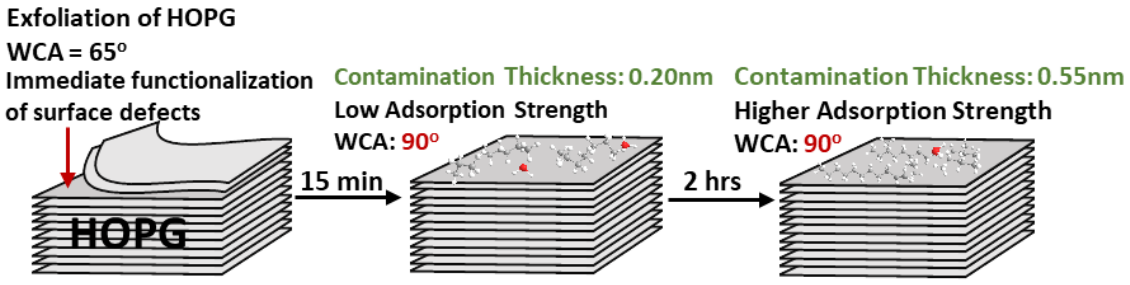

Figure 17. Illustration of the dynamic airborne contamination process as observed for HOPG.

3.5 Conclusions

We have studied the time evolution of airborne contamination composition on HOPG using UPS. He II UPS is a sensitive spectroscopy tool to probe the early stage contamination of the HOPG surface and provides a clear advantage over XPS in terms of differentiation between carbons in different chemical states. A time-dependent change in the composition of the adsorbate was observed. Comparison of UPS spectra of HOPG exfoliated in air with that in UHV shows an instantaneous change in the surface composition, which we attribute to functionalization of active surface defects of HOPG in air. Our data further suggests that the contaminants adsorbed during short term air exposures are primarily low-molecular-weight or weakly-bound species that desorb in UHV. Additionally, as air exposure time was increased, larger and more strongly bound contaminants were observed on the surface. A representation of this is shown in Figure 17. Our results provide insights into the chemical composition of the dynamic contamination layer, which has not been previously reported in the literature. Clean carbon materials show significantly improved electrochemical and energy storage properties compared to their contaminated counterparts.[38, 132] We hope that a better understanding of the early stage and long term dynamics of airborne contamination of HOPG will aid the development of technologies that prevent and/or reverse the contamination of graphitic materials.

4.0 Mechanical Properties of Macroscale CVD Graphene Fibers

4.1 Chapter Preface

A research manuscript based on portions of the material included in this section is in preparation for submission.

List of Authors: Muhammad Salim, Luke Thimons, Mina Kim, Brennan Carr, Michelle Montgomery, Nathan Tolman, Tevis Jacobs, Haitao Liu

Author Contributions: M.S. developed the initial idea and experimental design. M.S., L.T., M.K., T.J., and H.L. designed and directed experiments. M.S., L.K., and M.K. conducted the experiments. All authors discussed the results and M.S. and H.L. co-wrote the manuscript with input from authors.

4.2 Background

Since the discovery of graphene, researchers have investigated its remarkable electrical, thermal, chemical, and mechanical properties. Graphene forms the basis of both graphite and CNTs, and its intrinsic strength has been predicted to exceed that of any other material.[133] Although there have been several nano-scale experimental studies on the mechanical properties of graphene and CNTs, the materials' properties have not yet been measured sufficiently.[44, 48, 50, 134-136]

Nano-indentation measurements on graphene reveal a high elastic modulus (E=1.02 TPa), and intrinsic strength (σ_{int}=130 GPa), making graphene a promising material.[50, 136] With such remarkable mechanical properties coupled with its specific surface area (2630 m^2/g), graphene based reinforcements have been shown to enhance composites.[41, 134] CNTs show a reduced mechanical behavior, compared to that of graphene, primarily because of the increased presence of intra- and inter- layer defects formed during the fabrication process.[42-48] The limitations imparted by these defects ultimately results in a lower tensile strength and elastic modulus than its graphene relative.[44, 137-138]

Nano-scale tensile tests of free-standing SWCNTs and MWCNTs have revealed an intrinsic strength of ~30GPa and an elastic modulus of ~500-1000GPa.[44, 139] MWCNT measurements were shown to be equivalent to the of mechanical testing on a single SWCNT with a diameter equal to the MWCNT diameter, this is a result of poor load transfer between CNT layers in MWCNTs.[44, 140]

Macro-scale measurements on MWCNT bundles have shown vastly different properties to their nano-scale counterparts, with a tensile strength of 1.72 GPa and an elastic modulus of 0.45 TPa for lengths of ~2 mm.[141] Others have reported a tensile strength of 1.2 GPa and elastic

modulus of 16 GPa for double-walled CNT bundles for lengths of ~10 mm.[142] Macro-scale measurements on SWCNTs also show the same reduced mechanical behavior to their nano-scale measurement counterpart, with a tensile strength of 1.0 GPa and an elastic modulus of 49 to 77 GPa for lengths of ~200 mm.[143] The mechanical properties reported by macro-scale measurements are much lower in magnitude than for measurements performed on the nano-scale, which is presumed to be due to the much longer lengths of CNTs tested on the larger scale—in that a much longer CNT may be more likely to have a critical defect that could lead to a failure present somewhere along their length.[44, 141]

Although the dependence of fracture strength on length has not yet been experimentally addressed for CNTs, Griffith et al. deduced that the actual breaking strength of a brittle material is governed by the defects and flaws within the material, rather than the intrinsic strength of its atomic bonds. To emphasize this, Griffith proceeded to experimentally measure the breaking strength of a series of glass fibers with progressively smaller diameters, observing a general increase in tensile strength with smaller diameters. [144] This conclusion can be applied to CNTs and graphene, where mechanical measurements performed on larger-scale (e.g., macro) samples produce lower tensile strengths and elastic moduli than those performed on smaller scales (e.g., nanoscale).

Although the influence of defects on the macro-mechanical properties of graphene has not yet been investigated experimentally, it can be expected that point defects, in particular vacancies, will decrease the elastic modulus and tensile strength of graphene, based on the theoretical and experimental data provided by CNTs.[145] Herein, we present the first study to perform sequential macro-scale tensile tests on polymer-free graphene fibers, and report the vastly superior macro-mechanical properties and accessibility offered by macro-scale graphene fibers in comparison to current macro-scale CNTs.

4.3 Materials and Methods

4.3.1 Graphene Synthesis

Graphene was grown on copper foil (25 μm thick, Alfa Aesar, item No.46365) using a CVD method previously reported.[146] First, copper foil was electropolished similar to the previously reported electropolishing method.[147] In brief, copper foil is electrolyzed at 8 V with the current limit of 0.45 A for 30 – 45 s in phosphoric acid solution (500 ml of deionized water, 250 ml of phosphoric acid, 250 ml ethanol, 50 ml isopropyl alcohol, and 5 g of urea). Copper foil was used for both anode and cathode electrode, but only polished anode copper foil was used for graphene growth. After the electropolishing treatment, copper foil was thoroughly rinsed with deionized water, blow dried with nitrogen gas, and placed on a quartz boat. The quartz boat with the copper foil was then inserted into the center of a 1-inch-diameter fused quartz tube furnace. The tube was pump down to the base pressure ~50 mTorr and back filled with H_2 (10 standard cubic centimeters per minutes (sccm)). The tube pressure with H_2 flow was maintained at ~500 mTorr. The furnace temperature was ramped to 1050 °C and annealed for 1 h. CH_4 (2 sccm, P_{total} ~750 mTorr) was introduced after the annealing step for 30 min (growth), and the furnace was cooled rapidly to room temperature with the same gas flow. Figure 18 summarizes the CVD growth process. Graphene samples were stored in a clean glass petri dish until the transfer.

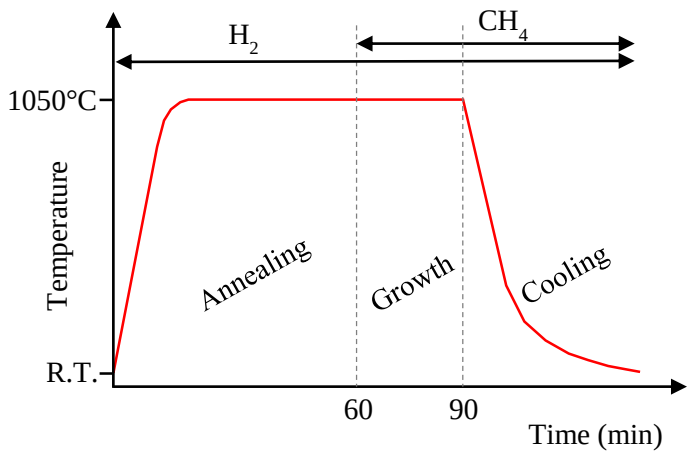

Figure 18. The CVD growth of graphene. Furnace temperature was set to 1050 °C. Annealing and growth period was 60 min and 30 min, respectively. H_2 and CH_4 flow rate was set to 10 sccm and 2 sccm, respectively. The quartz tube had base pressure of ~50 mTorr after evacuation, ~500 mTorr with H_2, and ~750 mTorr with H_2+CH_4.

4.3.2 Raman Spectroscopy of CVD Grown Graphene

CVD grown graphene was transferred on to a silicon wafer using a wet transfer technique and characterized via Raman spectroscopy. Micro-Raman spectra were obtained using Horiba scientific XploRA PLUS with Olympus Microscope BX41 with 100X (NA:0.9, WD:0.21mm) objectives. 473nm (20-25mW) continues wave laser with 10 % density filter and 1800 gr/mm grating were used. Slit and pin hole size was 100 µm and 300 µm, respectively. Laser power and acquisition time settings were adjusted to prevent the oxidation of graphene from the laser induced heating effect. Typical Raman spectrum of graphene is shown in Figure 19. The negligible D peak intensity, low intensity ratio between the G peak and the 2D peak (I_G/I_{2D}), and narrow linewidth

of the 2D peak suggest that the CVD graphene used in this study is mostly single layer and have low defect density.[148-149]

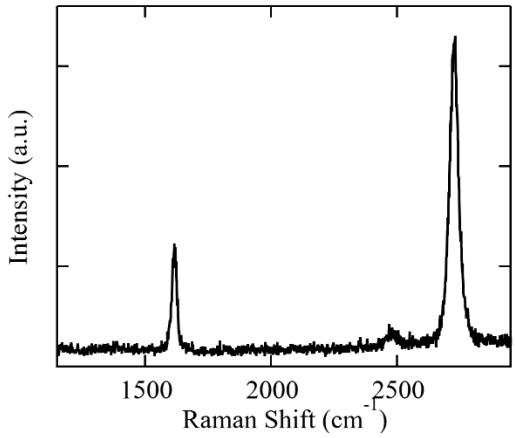

Figure 19. The Raman spectrum of graphene on SiO_2/Si wafer.

4.3.3 Graphene Transfer on Si Wafer

In a typical transfer, as grown graphene on top of Cu foil was spin coated with 5 wt% PMMA solution (PMMA, Aldrich, MW 996000 in anisole, Sigma-Aldrich, 99%). After the PMMA was coated on top of the graphene layer, the Cu foil was etched in etchant solution, 1 M of iron chloride in 10 % w/w hydrochloric acid ($FeCl_3$, Sigma-Aldrich, 97%, in HCl, Fisher Scientific, 37.1%) for 30 min. Then, the PMMA/graphene film was scooped out with a clean glass slide and transferred into multiple water baths to rinse off the etchant. After thorough rinsing, the PMMA/graphene film was scooped on a SiO_2(300nm)/Si wafer (University Wafer, 300 nm wet thermal oxide, P type/Boron) and spin dried at 5000 rpm for 5 min. The PMMA layer was removed by placing the sample in an acetone bath for 1 h. The graphene surface was rinsed with isopropanol and gently blow dried with N_2.

4.3.4 Fabrication of Graphene Rope

Graphene rope was assembled by folding flat sheet of graphene on a glass slide. In a typical assembly, graphene/Cu was spin coated with 3-5 wt% PMMA solution and Cu foil was etched as described above. The PMMA/graphene film was rinsed in water bath and placed on a clean glass plate. Then the film was pushed horizontally with clean glass slides to form a folded structure. All glass plate and slides were thoroughly cleaned and treated with UV/O_3 (PSD Pro Series UV-Ozone System, Novascan) for 1 hr to increase the wetting property before use. The schematic drawing of folding process is shown in Figure 20.

To remove PMMA, folded PMMA/graphene rope was heated beyond the thermal decomposition temperature of PMMA (390 °C).[150-151] First, PMMA/graphene rope was suspended on a copper foil and placed in a quartz tube. Once the tube was evacuated (P ~ 50 mTorr), PMMA/graphene rope was heated to 420 °C for 30 min in Ar (P > 1 Torr). The system was cooled to room temperature, and graphene rope was stored in a plastic petri dish until further testing.

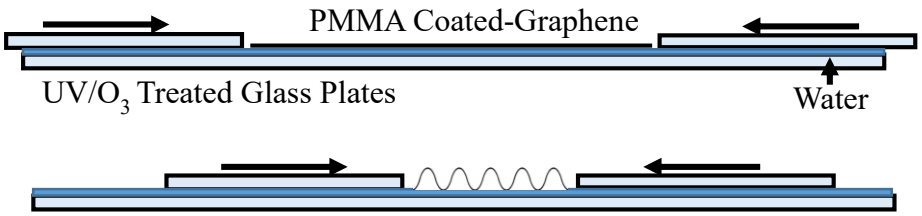

Figure 20. Schematic of folding process for PMMA-Coated Graphene. Glass plates were treated by UV/O_3 prior to wetting or graphene transfer onto plate. Wrinkles formed in the graphene sheet during compression, and remained folded as the sheet was compressed further**.**

4.3.5 Characterization Methods

Graphene rope was characterized by field-emission Scanning Electron Microscopy (SEM) using a Zeiss Sigma 500 VP SEM. Conductive silver paste (Silver Conductive Adhesive 503, Electron Microscopy Sciences) was added over the non-conductive epoxy or crystal bond adhesives to eliminate charging during the SEM imaging of graphene fibers.

4.3.6 Tensile Test Setup

Tensile measurements were collected using a custom-made tensile testing setup, shown schematically in Figure 21. The setup employed a cantilever beam of known stiffness (882 N/m) coupled with a capacitive displacement sensor (Physic Instrumente, D-510.010) to measure applied force with an accuracy of +/- 25 μN. A newly fabricated graphene fiber, which still anchored to the copper substrate where it was annealed, had one end of it raised into a droplet of epoxy (Devcon No. 14250) on the tip of the cantilever via a three-axis stage (Aerotech MPS75SL-V)—the epoxy was allowed 45 min to 1 hour to harden before testing. Sequential measurements

on the same mounted graphene fiber were performed by lowering the newly broken end of the graphene fiber into a pool of crystalbond mounting adhesive (Ted Pella 509-3) (heated to 150°C, past its softening point). Ideally the samples would be aligned perfectly vertically, parallel to the loading axis. In the case of the experiments done, this was generally not the case, further angle details are provided in the results.

The experimental setup was positioned on a vibration isolation table (Kinetic systems minus K) in ambient conditions (22 ˚C and 20-30% relative humidity).

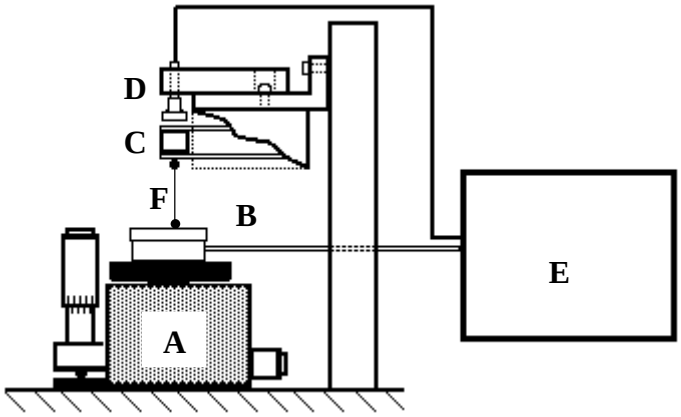

Figure 21. (A)Testing setup for contact tests depicting the three-axis motor-driven stage; (B) the piezoelectric actuator; (C) the cantilever with bead of epoxy; (D) the capacitive sensor; (E) and the corresponding controls; (F) graphene fiber mounted with beads of adhesive.

4.3.7 Uniaxial Tensile Test Procedure

Once the graphene fiber was mounted, as indicated above, and adhesives had hardened, the three-axis motorized stage was lowered. This movement created a tensile load on the sample which was registered by the cantilever beam/capacitive sensor. The loading occurs at rates (r_p) varying between 0.1 – 2 μm/s until fracture, with data sampling at (1000 data points/sec). The displacement of the stage was recorded along with the displacement and corresponding force of the cantilever beam. The stage was lowered until fracture was observed. The broken samples were preserved for later SEM imaging. After fracture, another test was carried out on the graphene fiber still attached to the epoxy on the cantilever beam. The broken end was then lowered into liquid crystalbond adhesive on the stage. Again, the crystalbond was allowed to harden completely before applying any load to the sample. After each fracture, the new, shorter sample was reattached to a

new pool of crystal bond adhesive on the stage, allowed to harden, and then pulled until fracture. This process was repeated until the sample was too short to test again.

4.3.8 Data Collection

Data was collected on the stage displacement and the force exerted on the sample with respect to time by using a National Instruments DAQ unit (NI USB-6009) and the LabView development environment. Video and pictures were taken for each test with a digital microscope (Dinolite AM4515ZTL). This setup allowed for strain data to be extracted from the video and total mechanical failure to be observed. Such data was gathered several times for each sample over the course of multiple tensile tests.

The mounted graphene fibers were typically set an angle (0-45° to vertical) due to restrictions in fabrication and mounting. Any load in the rope where the sample is straight will be along the axis of the rope. If it doesn't break at the bends in the sample, then the entire load is supported along the axis of the rope. Since we are only measuring vertical deflection (force), the value we are getting should be an underestimate of the real force experienced by the rope, which will also cause some horizontal deflection. Additionally, the fibers were usually slightly bent or kinked along their axis. Therefore, displacements measured during testing are affected by both the angle of setting and bends/kinks along the fiber axis. Force-Time plots was used (over F-ΔD plot) to help display the data due to these issues. Stress-strain curves were generated by measuring distances between reference points on the graphene fiber at instantaneous moments during the test by digital imaging.

4.4 Results

4.4.1 Tensile Tests of Graphene Fibers

The dimensions of the macro-scale graphene fibers were based upon the size of CVD graphene sheet used to make them. In this sense, the length and cross-sectional area of the graphene fibers could be controlled by using different sizes of CVD graphene sheets for fabrication. SEM images of the graphene fiber after annealing to remove PMMA (Figure 22A-B), and after tensile testing (Figure 22C-D). The typical nominal diameter of the fibers post-annealing was between 15-80 μm. The length of the graphene fibers (L_{fiber}), after fabrication, was measured with a digital microscope and were typically in the 0.1-2 cm range, Figure 23.

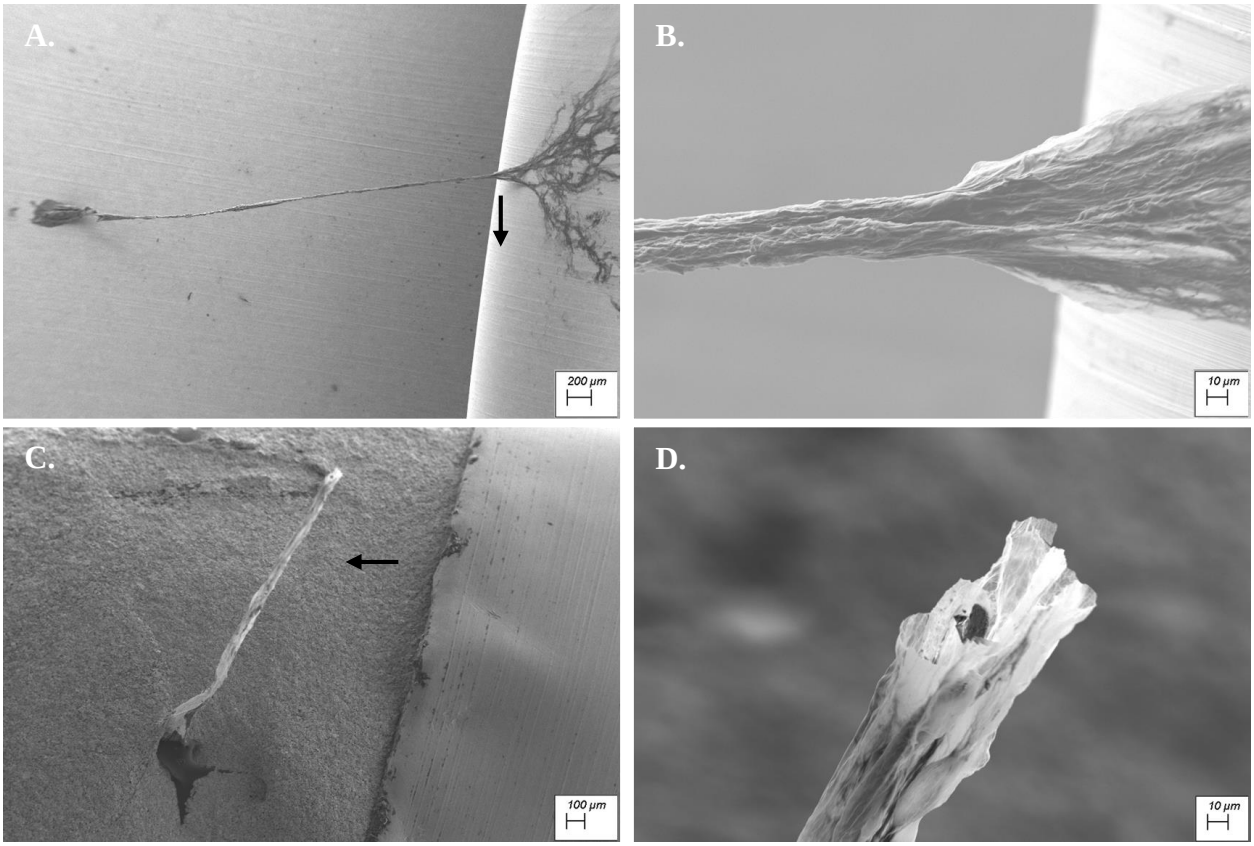

Figure 22. SEM images of graphene fibers. **(A)** suspended graphene fiber after annealing on copper substrate to remove PMMA. **(B)** magnified region of **A**, marked with arrow. Diameter (d) = 20 µm. **(C)** a graphene fiber, mounted in adhesive, after breakage during tensile testing. Adhesive is coated in conductive silver paste for imaging. **(D)** magnified region of **C**, marked with arrow, d = 30 µm.

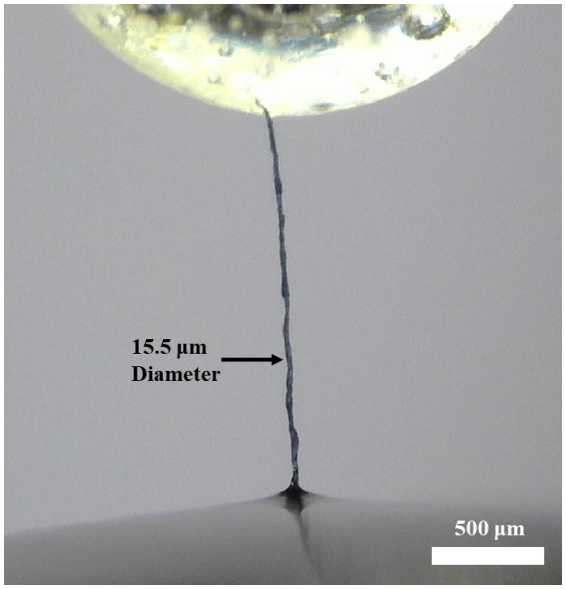

Figure 23. Digital microscope image of a graphene fiber mounted to piezoelectric stage and to epoxy bead on cantilever.

In order to determine the *E* value of the graphene fiber ($E=\Delta\sigma/\Delta\varepsilon$), the F-time(t) plot (Figure 24, Bottom) was transformed into a stress-strain (σ-ε) curve. Strain ($\varepsilon=\Delta L/L$) was calculated by measuring ΔL as described in the methods. To calculate the stress ($\sigma=F/S_{eff}$), S_{eff} was calculated by using the width (along the compression folding axis) of the CVD graphene sheet used to form the fiber and thickness of graphene (0.335 nm). For a 1 cm wide CVD graphene sheet, the ideal cross-sectional area is 3.35 μm^2.

Uniaxial testing was performed for a series of graphene fibers with varying S_{eff} and L_{fiber}. For each fiber, tests were performed until fracture, with further consecutive tests performed on the new broken segments. Figure 24 shows the tensile testing for graphene fiber with a cross-sectional area of S_{eff}=1.84 μm^2 and L_{fiber}=550 µm, this was the third consecutive tensile test performed on the fiber.

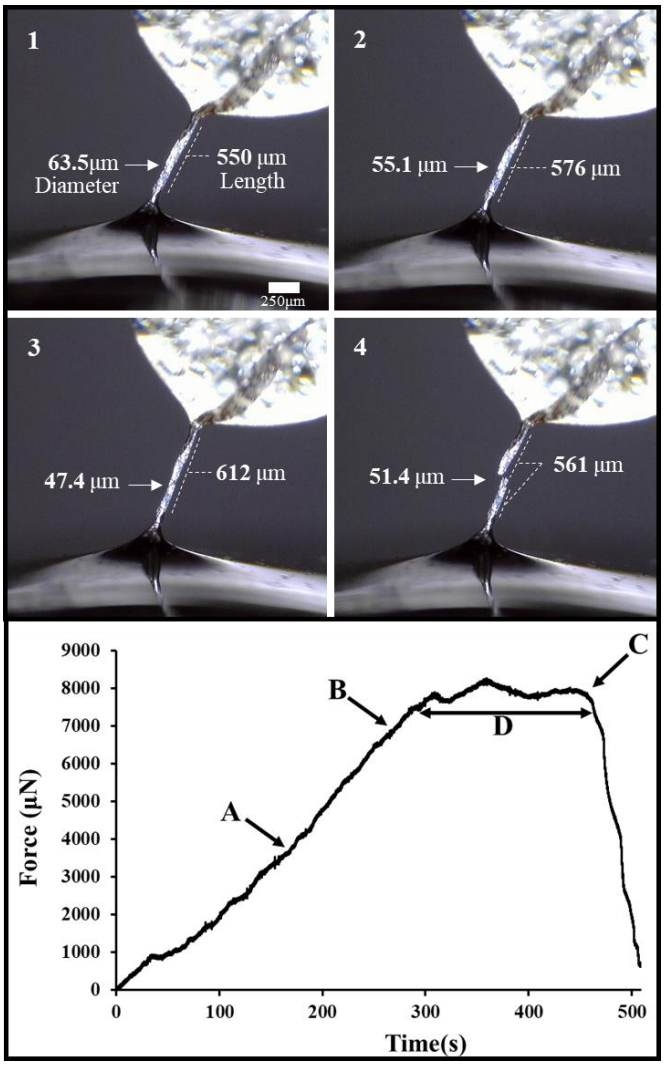

Figure 24. Tensile testing and failure of graphene fiber (S_{eff}=1.84 μm^2, r_p=0.50 μm/s) **Top:** Four frames **(1-4)** of a graphene fiber tensile test. **(1)** Graphene fiber dimensions(t=166s, d=63.5 μm, L_{fiber}=550 μm) after straigtening from bends/kinks in the structure **(Position A)**; **(2)** Maximum yield stress. (t=264 s, d=55.1 μm, L_{fiber}=576 μm), **(Position B)**; **(3)** Pre-fracture (t=464 s, d=47.4 μm, L_{fiber}=612 μm), **(Position C)**; **(4)** Post-fracture (t=520 s, d=51.4 μm, L=561 μm). **Bottom:** F-t plot of graphene fiber depicted in **Top**. **A-B** represents region in **Figure 25** used for calculation of *E*. **C** Points to the fracture initation of the graphene fiber. The maximum force at this point can be used to calculate tensiel strength. Graphene fiber fractures in an unzipping pattern, which is observed by video and by the gradual (rather than immediate) reduction to F=0 μN. **(D)** Region of creep deformation on graphene fiber.

Top of Figure 24 (1-4) depicts four time-stamped frames during the tensile testing. Frame 1, with initial starting diameter (D_{fiber}=63.5 μm) and (L_{fiber}=550 μm), was taken most bends along the axis were removed by the axial test movement, forming a more linear fiber. Changes in D_{fiber} and L_{fiber} from this point are a combination of further unbending and elastic or plastic deformation along the fiber. Frame 2 is at the maximum yield stress, where the with dimensions of D_{fiber} changed by -4.9% and L_{fiber} by +15.5% by this point. Frame 3 is right before graphene fiber fracture and breaking, when D_{fiber} is at its minimum (-14.0%) and L_{fiber} (+11.4%) at its maximum during testing. Maximum stress, σ_b, calculated at this point is 2.6 GPa. The true stress is not quite uniform throughout the fiber, and there is always some location, perhaps a nick or some other defect at the surface, where the local stress is maximum. Frame 4 is after fracture, where the final dimensions of D_{fiber} and L_{fiber} were changed by -6.6% and +2.2% relatively—these changes after fracture were constant, suggesting a similar amount of plastic deformation. Therefore, by removing the plastic deformations from the maximum deformations during testing of the graphene fibers, the total elastic axial changes are calculated to be 9.2% of initial L_{fiber}. The stress-strain curve for this test is shown in Figure 25, with a measured *E* value of 61.85 GPa ± 2.26 GPa.

Fracture initiation on the graphene fibers was observed to occur near maximum load, whereby the propagation of the fracture across the width of the graphene correlated with a plateauing of the measured force. The crack propagation occurred in an unzipping pattern, which has been previously suggested to favor directional behavior along grain boundaries and defects. Hwangbo et al. also reported that the fracture mechanics of graphene is influenced by the surrounding environment, particularly atmospheric moisture.[152] In this sense, the fracture mechanics may be understood as a single-sheet parallel of stress-crack-corrosion (SCC).

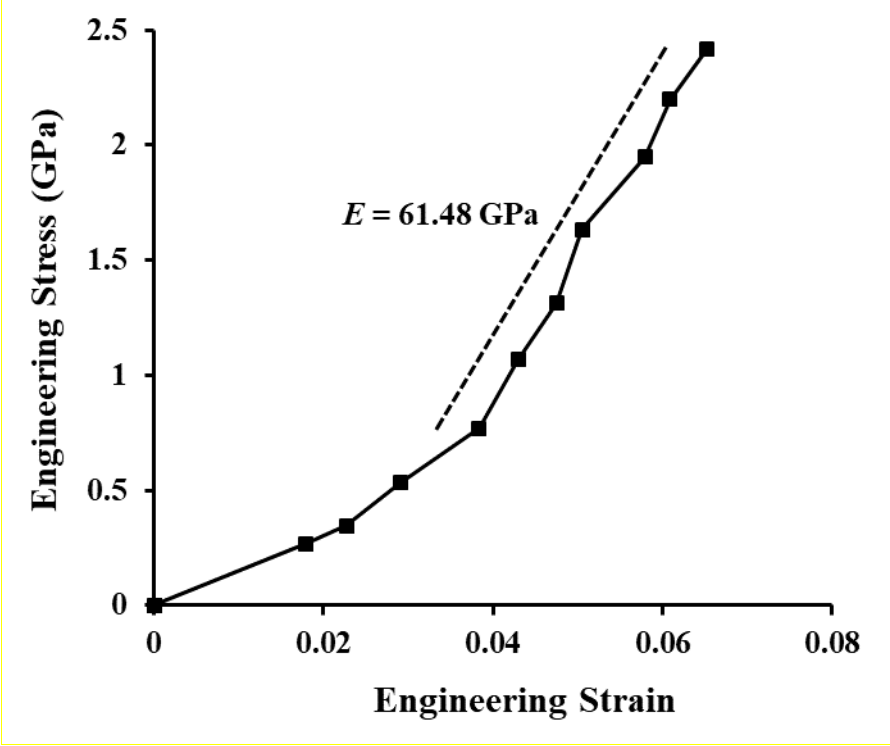

Figure 25. The uniaxial stress applied to the graphene fiber vs the strain (elongation). The fitted line's slope gives a Young's modulus value of 61.48 GPa.

4.4.2 Sequential Tensile Tests

Maximum tensile strength was calculated for each graphene fiber and resulting fragments and were measured sequentially after each break. Three different graphene fibers, and corresponding tensile strengths for the length of the initial fiber, and fragments, are shown in Figure 26. A gradual increase of σ_b was observed for sequential tensile measurements, where the longest fiber had the lowest σ_b, and the shortest fragments had the largest σ_b. The enhanced σ_b for smaller fragments are most likely due to the combination of two effects: 1. Fragments are formed when a larger fiber is broken through testing. The initiation of a fracture will most likely occur at the fiber's most critical defect. Therefore, the resulting fragments formed would logically have a greater strength, since the most critical defect was removed during the formation of the fragments. 2. A smaller graphene fiber would be less likely to have a critical defect, which could lead to a failure, present somewhere along its length.

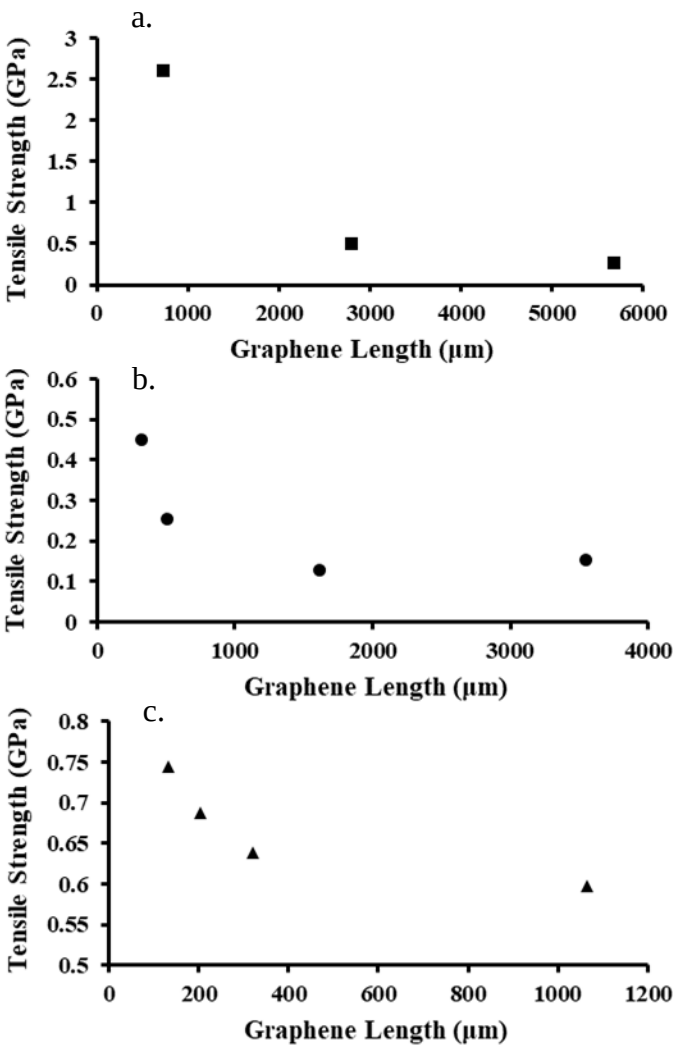

Figure 26. Tensile strength of three different graphene fibers (A, B, and C) as a function of fiber fragment length. **(A)** S_{eff}=3.2µm^2. **(B)** S_{eff}=2.8µm^2. **(C)** S_{eff}=5.2µm^2.

4.4.3 Conclusions

We have measured the intrinsic strength and elasticity of CVD graphene fibers by uniaxial tensile tests. The values of σ_b measured contained a large variation about the average 0.65 GPa ± 0.59 GPa, a product of σ_b varying with sequential tensile tests. Typically, the σ_b measured on the shortest fiber fragment after sequential tensile tests was in the range of 0.5-2.0GPa, with the largest measured value being 2.6GPa. This is the largest intrinsic tensile strength reported for any graphene, graphite, or CNT fiber on the macro scale. The average *E* value measured was 53.2 GPa ± 0.59 GPa, comparable to other reported values for macro-scale CNTs.[143] Furthermore, our data suggests that the intrinsic strength of graphene fibers is a function of graphene length, which may explain the large discrepancy of reported σ_b between nano- and macro- measurements for CNTs.

5.0 Outlook

In summary, my work provides substantial insight into the dynamics of airborne contamination of REOs and graphitic surfaces. These results could have significant implications on the fundamental understanding of surface-sensitive properties and applications on these and other materials. The mechanical properties of novel macro-scale graphene fibers are also explored, with future work planned toward the goal of measuring the intrinsic tensile strength and elastic modulus of macro-scale graphene. This will be accomplished by further decoupling detrimental graphene-graphene interactions, by using free-flow coatings, and enhancing mechanical properties through the manipulation of grain sizes.

Appendix A

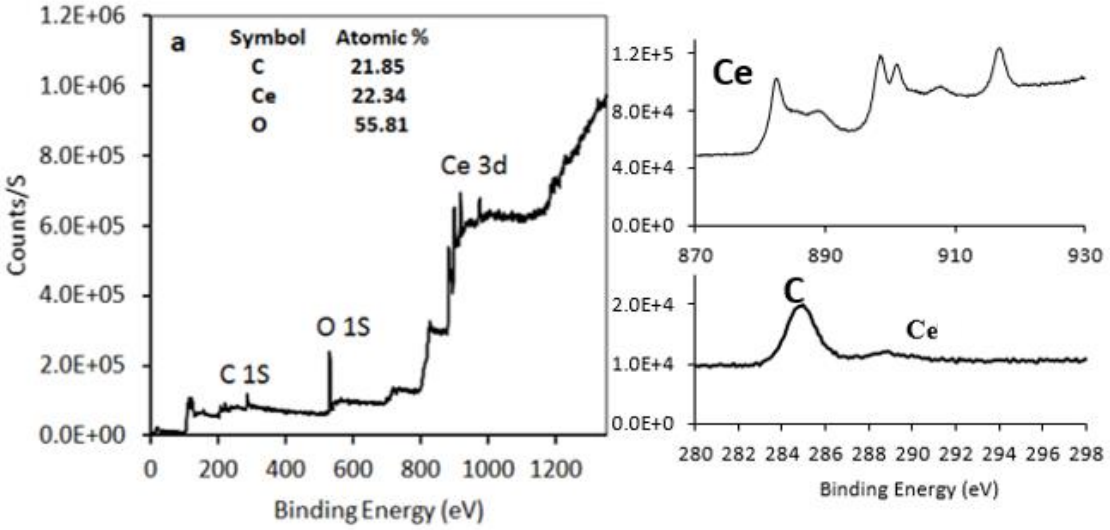
a
Symbol Atomic %
C 21.85
Ce 22.34
O 55.81
Ce 3d
O 1S
C 1S
Counts/S
Binding Energy (eV)
Ce
C
Ce
Binding Energy (eV)

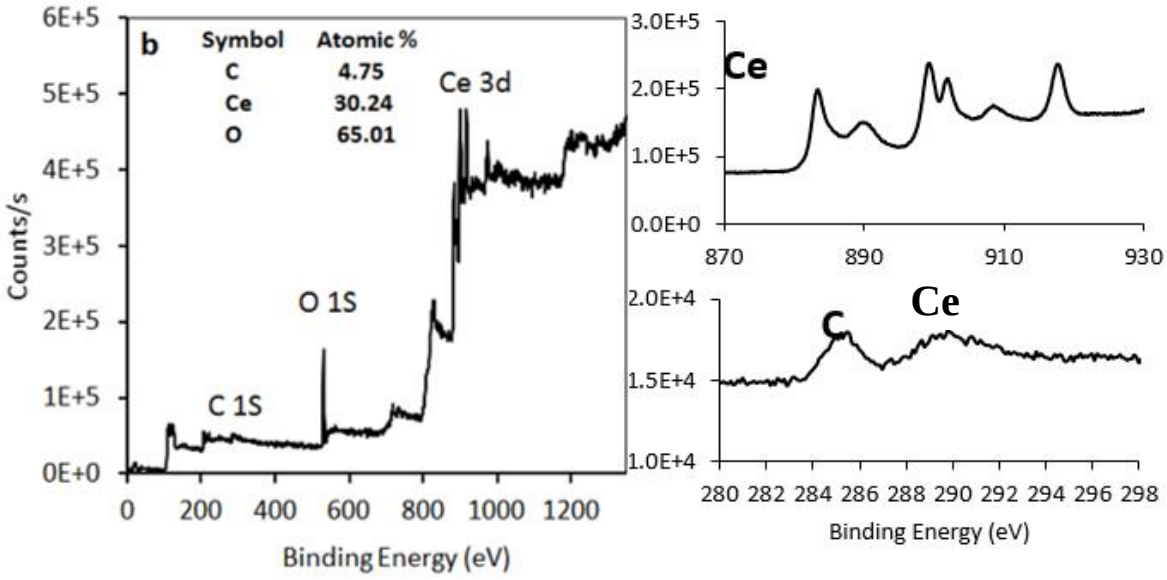
b
Symbol Atomic %
C 4.75
Ce 30.24
O 65.01
Ce 3d
O 1S
C 1S
Counts/s
Binding Energy (eV)
Ce
C
Ce
Binding Energy (eV)

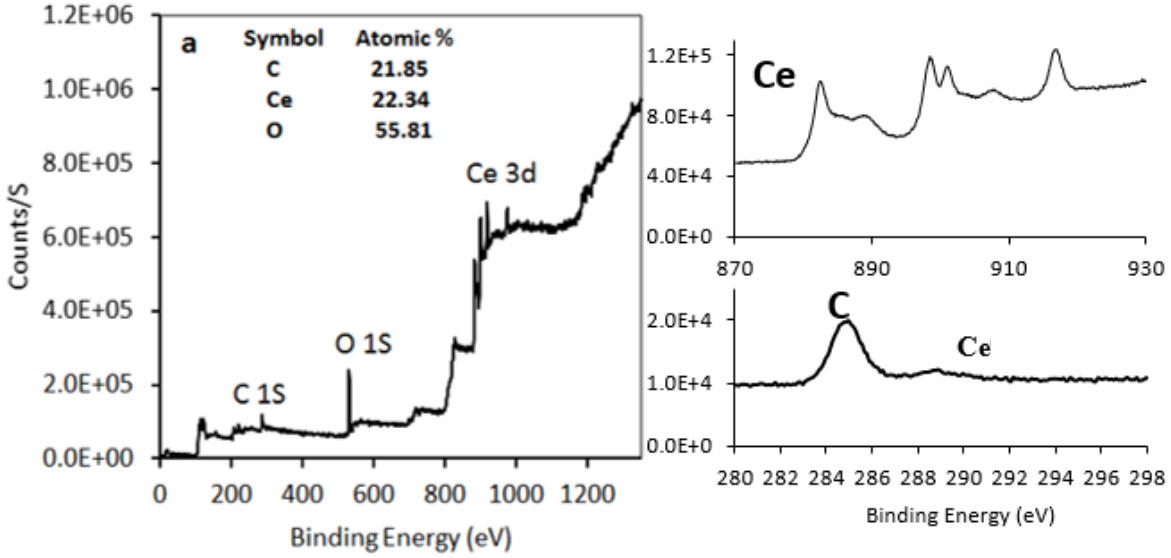
a
Symbol Atomic %
C 21.85
Ce 22.34
O 55.81
Ce 3d
O 1S
C 1S
Counts/S
Binding Energy (eV)
Ce
C
Ce
Binding Energy (eV)

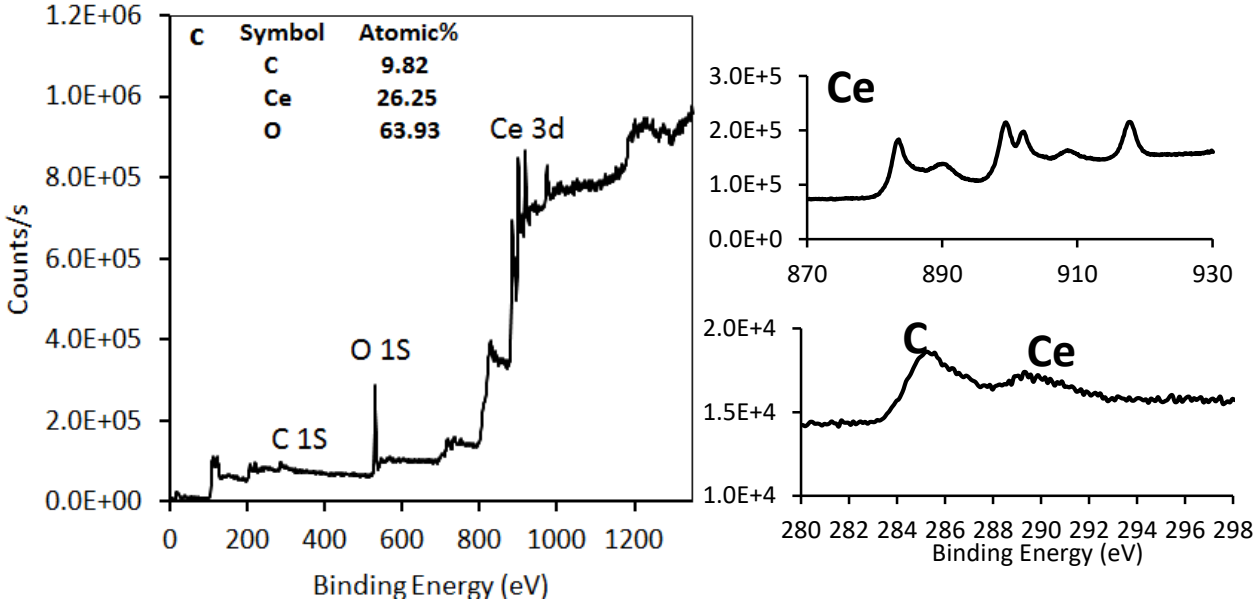
c
Symbol Atomic%
C 9.82
Ce 26.25
O 63.93
Ce 3d
O 1S
C 1S
Counts/s
Binding Energy (eV)
Ce
C
Ce
Binding Energy (eV)

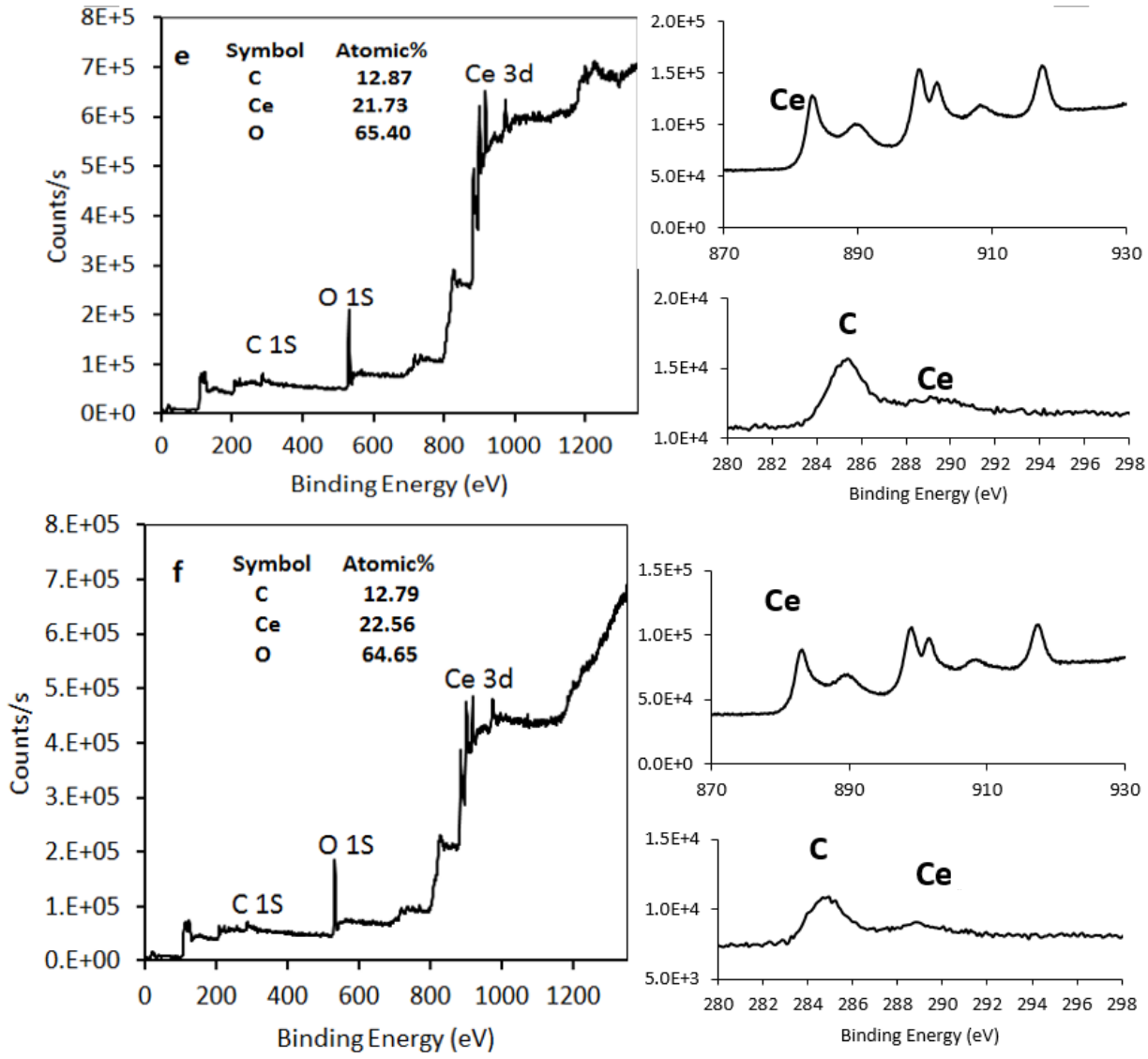

Figure 27. XPS Spectra of as-received and treated CeO_2 samples. | Survey spectra, as wel l as Carbon and Cerium spectra, are shown. a, As received; b, Annealed at 500 ^oC; c, Sample b stored in ambient air for 24 hours; d, Sample b stored in UHV XPS chamber for 24 hours; e, Sample c stored in ambient air for 2 weeks; f, Sample d stored in ambient air for 2 weeks.

Appendix B

AFM Imaging. AFM images were taken with tapping mode in air using an Asylum Research MFP-3D Atomic Force Microscope. Silicon HQ:NSC15/Al BS (325 kHz, 40 N/m) probes were used and purchased from μmasch (NanoandMore, USA). All images were taken at a scan rate of 0.50 Hz at 256 points per line. Each image required approximately 8 minutes to collect. HOPG aging from 45 seconds to 2 hours after exfoliation was done under the instrument cantilever holder to maintain the same scan area. HOPG aging beyond 2 hours took place inside a glass vial resting on its side to prevent larger particulate matter from landing on the HOPG surface. Surface morphology changes by VOC contamination during air exposure were not detectable by AFM.

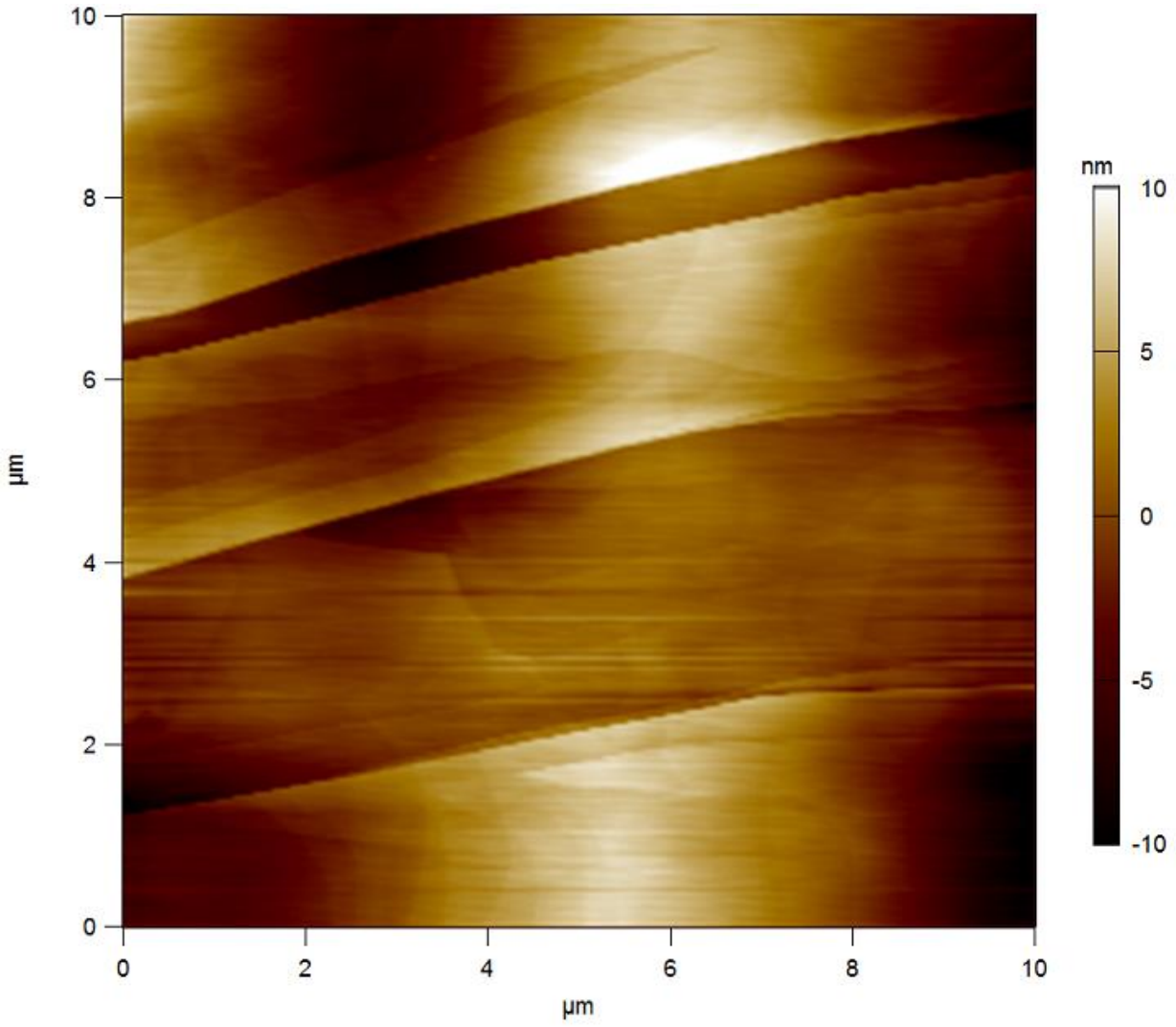

Figure 28. HOPG aged 45 seconds.

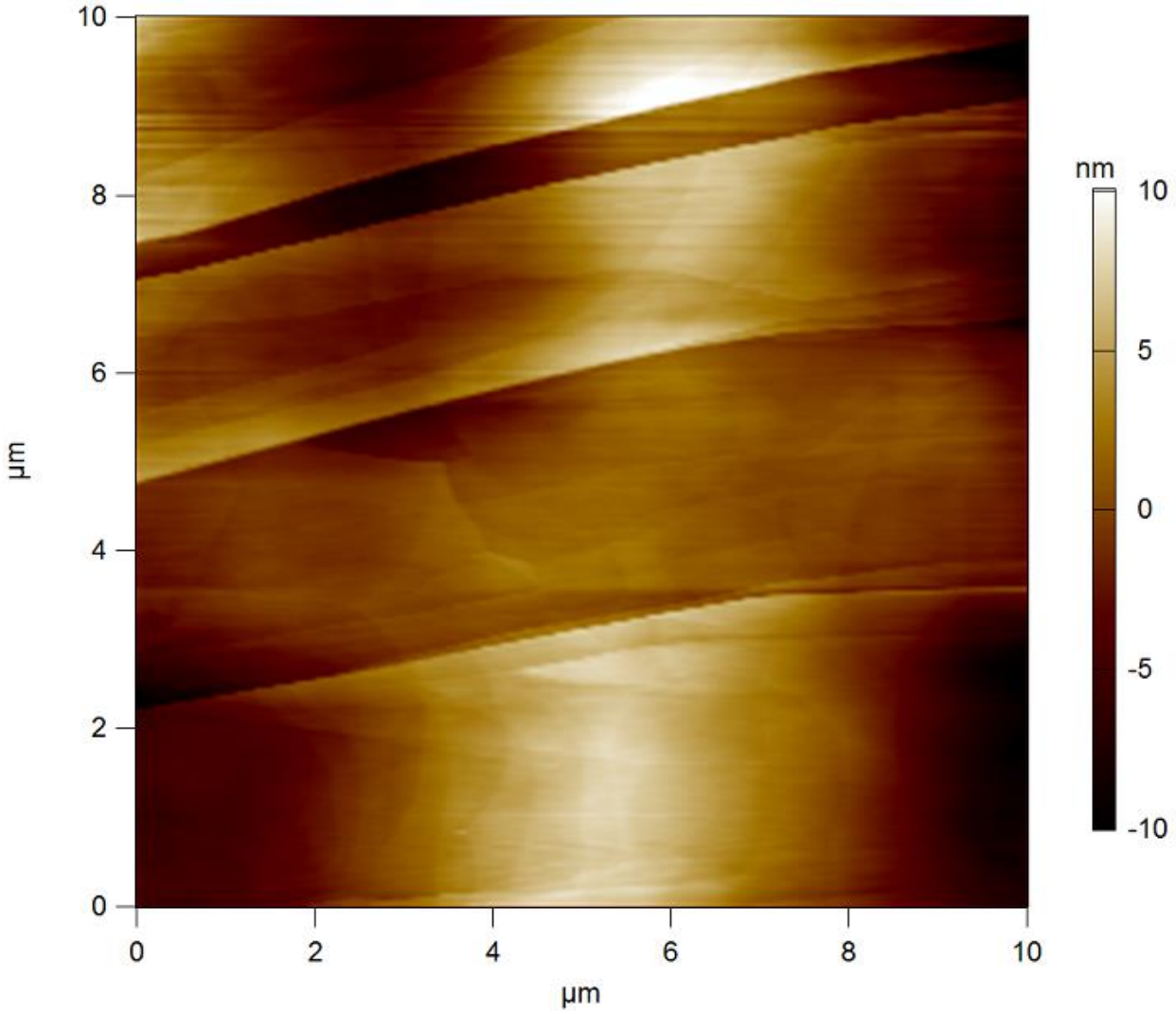

Figure 29. HOPG aged 2 hrs.

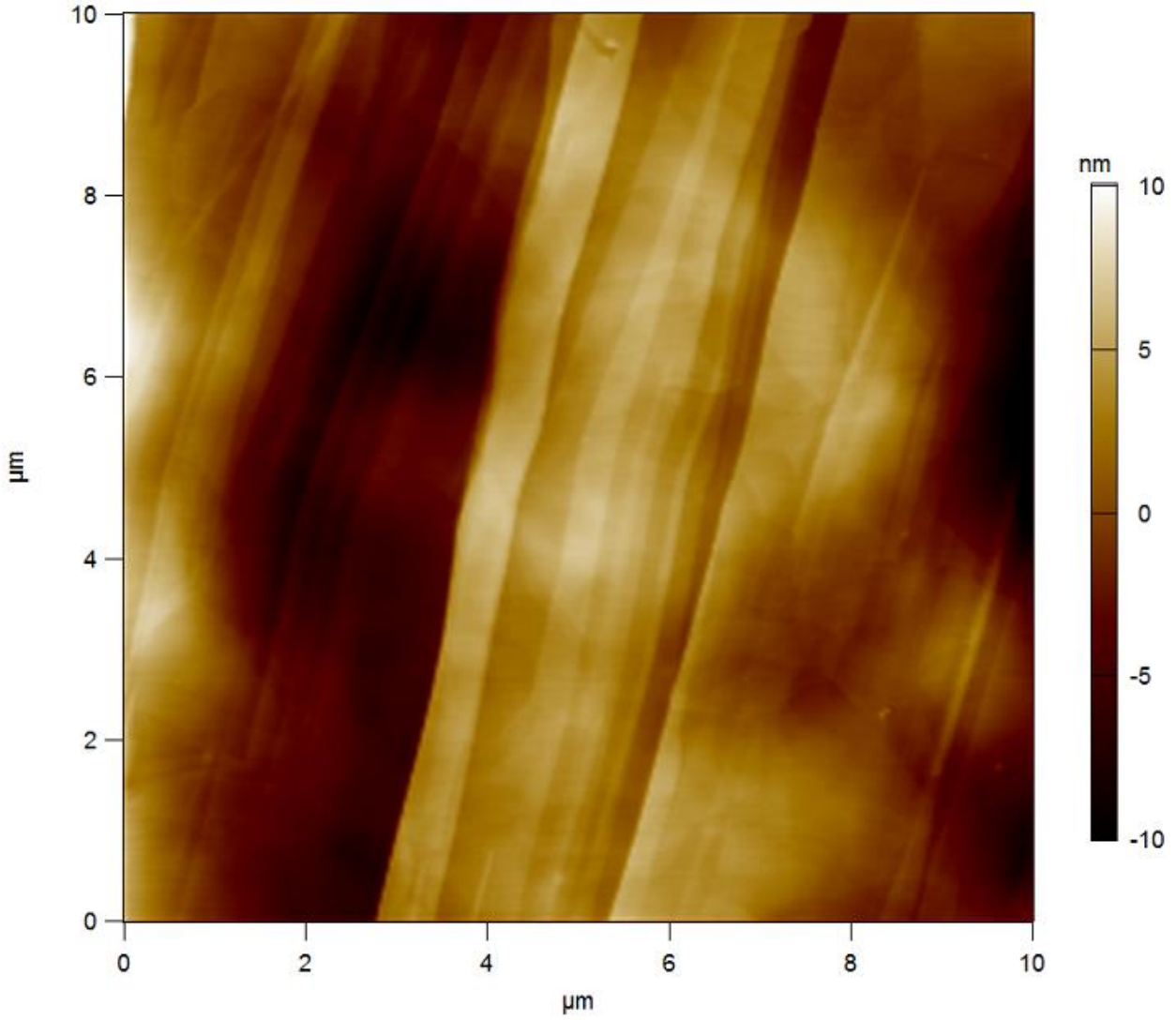

Figure 30. HOPG aged 24 hours.

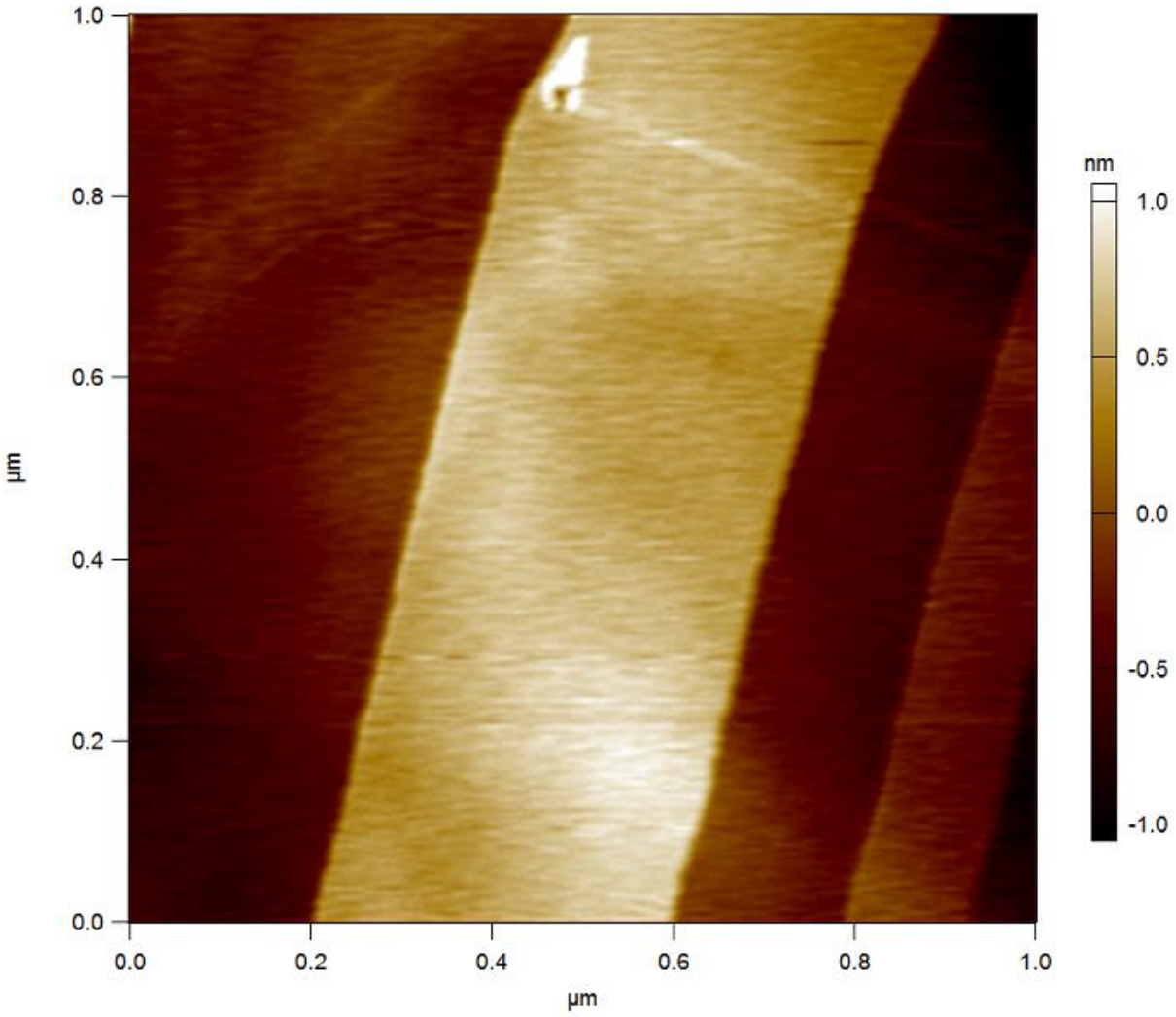

Figure 31. Close up of step edges of the HOPG sample aged 24 hours.

Bibliography

[1] Fanelli, D., Opinion: Is science really facing a reproducibility crisis, and do we need it to? *Proceedings of the National Academy of Sciences* **2018,** *115* (11), 2628-2631.

[2] Li, Z.; Wang, Y.; Kozbial, A.; Shenoy, G.; Zhou, F.; McGinley, R.; Ireland, P.; Morganstein, B.; Kunkel, A.; Surwade, S. P.; Li, L.; Liu, H., Effect of airborne contaminants on the wettability of supported graphene and graphite. *Nature Materials* **2013,** *12*, 925.

[3] Fowkes, F. M.; Harkins, W. D., The State of Monolayers Adsorbed at the Interface Solid—Aqueous Solution. *Journal of the American Chemical Society* **1940,** *62* (12), 3377-3386.

[4] Morcos, I., On contact angle and dispersion energy of the cleavage graphite/water system. *Journal of Colloid and Interface Science* **1970,** *34* (3), 469-471.

[5] Morcos, I., Surface Tension of Stress-Annealed Pyrolytic Graphite. *The Journal of Chemical Physics* **1972,** *57* (4), 1801-1802.

[6] Shin, Y. J.; Wang, Y.; Huang, H.; Kalon, G.; Wee, A. T. S.; Shen, Z.; Bhatia, C. S.; Yang, H., Surface-Energy Engineering of Graphene. *Langmuir* **2010,** *26* (6), 3798-3802.

[7] Westreich, P.; Fortier, H.; Flynn, S.; Foster, S.; Dahn, J. R., Exclusion of Salt Solutions from Activated Carbon Pores and the Relationship to Contact Angle on Graphite. *The Journal of Physical Chemistry C* **2007,** *111* (9), 3680-3684.

[8] Wang, S.; Zhang, Y.; Abidi, N.; Cabrales, L., Wettability and Surface Free Energy of Graphene Films. *Langmuir* **2009,** *25* (18), 11078-11081.

[9] Raj, R.; Maroo, S. C.; Wang, E. N., Wettability of Graphene. *Nano Letters* **2013,** *13* (4), 1509-1515.

[10] Amadei, C. A.; Lai, C.-Y.; Heskes, D.; Chiesa, M., Time dependent wettability of graphite upon ambient exposure: The role of water adsorption. *The Journal of Chemical Physics* **2014,** *141* (8), 084709.

[11] Ashraf, A.; Wu, Y.; Wang, M. C.; Aluru, N. R.; Dastgheib, S. A.; Nam, S., Spectroscopic Investigation of the Wettability of Multilayer Graphene Using Highly Ordered Pyrolytic Graphite as a Model Material. *Langmuir* **2014,** *30* (43), 12827-12836.

[12] Lai, C.-Y.; Tang, T.-C.; Amadei, C. A.; Marsden, A. J.; Verdaguer, A.; Wilson, N.; Chiesa, M., A nanoscopic approach to studying evolution in graphene wettability. *Carbon* **2014,** *80*, 784-792.

[13] Wei, Y.; Jia, C. Q., Intrinsic wettability of graphitic carbon. *Carbon* **2015,** *87*, 10-17.

[14] Mücksch, C.; Rösch, C.; Müller−Renno, C.; Ziegler, C.; Urbassek, H. M., Consequences of Hydrocarbon Contamination for Wettability and Protein Adsorption on Graphite Surfaces. *The Journal of Physical Chemistry C* **2015,** *119* (22), 12496-12501.

[15] Aria, A. I.; Kidambi, P. R.; Weatherup, R. S.; Xiao, L.; Williams, J. A.; Hofmann, S., Time Evolution of the Wettability of Supported Graphene under Ambient Air Exposure. *The Journal of Physical Chemistry C* **2016,** *120* (4), 2215-2224.

[16] Rouquerol, J.; Rouquerol, F.; Sing, K. S. W., *Adsorption by Powders and Porous Solids: Principles, Methodology and Applications*. Elsevier Science: 1998.

[17] Auroux, A., *Calorimetry and Thermal Methods in Catalysis*. Springer Berlin Heidelberg: 2013.

[18] Thomas, J. M.; Thomas, J. M.; Thomas, W. J., *Principles and Practice of Heterogeneous Catalysis*. Wiley: 2015.

[19] Haul, R., S. J. Gregg, K. S. W. Sing: Adsorption, Surface Area and Porosity. 2. Auflage, Academic Press, London 1982. 303 Seiten, Preis: $ 49.50. *Berichte der Bunsengesellschaft für physikalische Chemie* **1982,** *86* (10), 957-957.

[20] Attard, G.; Barnes, C., *Surfaces. English*. Oxford University Press: 1998.

[21] Kohli, R.; Mittal, K. L., Developments in surface contamination and cleaning. Vol. 6, Sources, generation, and behavior of contaminants. pp. 329-474.

[22] Kohli, R.; Mittal, K. L., Developments in surface contamination and cleaning. Vol. 6, Sources, generation, and behavior of contaminants. pp. 267-297.

[23] MacDonald, S. A.; Hinsberg, W. D.; Wendt, H. R.; Clecak, N. J.; Willson, C. G.; Snyder, C. D., Airborne contamination of a chemically amplified resist. 1. Identification of problem. *Chemistry of Materials* **1993,** *5* (3), 348-356.

[24] Hinsberg, W. D.; MacDonald, S. A.; Clecak, N. J.; Snyder, C. D., Airborne Contamination of a Chemically Amplified Resist. 2. Effect of Polymer Film Properties on Contamination Rate. *Chemistry of Materials* **1994,** *6* (4), 481-488.

[25] Zhao, E.; Dou, B.; Zhou, H.; Liu, S.; Chen, A. H.; Li, T.; Dai, G. In *Volatiel Organic Compounds Monitoring for Semiconductor Foundry Clean Room Air*, Indoor Air, 2005.

[26] Background Indoor Air Concentrations of Volatile Organic Compounds in North American Residences (1990 – 2005): A Compilation of Statistics for Assessing Vapor Intrusion. Agency, U. S. E. P., Ed. June 2011

[27] Hayeck, N.; Temime-Roussel, B.; Gligorovski, S.; Mizzi, A.; Gemayel, R.; Tlili, S.; Maillot, P.; Pic, N.; Vitrani, T.; Poulet, I.; Wortham, H., Monitoring of organic contamination in the ambient air of microelectronic clean room by proton-transfer reaction/time-of-flight/mass spectrometry (PTR–ToF–MS). *International Journal of Mass Spectrometry* **2015,** *392*, 102-110.

[28] Wu, C.-H.; Lin, M.-N.; Feng, C.-T.; Yang, K.-L.; Lo, Y.-S.; Jiunn-Guang, Measurement of toxic volatile organic compounds in indoor air of semiconductor foundries using multisorbent adsorption/thermal desorption coupled with gas chromatography–mass spectrometry. *Journal of Chromatography A* **2003,** *996* (1), 225-231.

[29] Meininghaus, R.; Gunnarsen, L.; Knudsen, H. N., Diffusion and Sorption of Volatile Organic Compounds in Building Materials−Impact on Indoor Air Quality. *Environmental Science & Technology* **2000,** *34* (15), 3101-3108.

[30] Tyson, W. R.; Miller, W. A., Surface free energies of solid metals: Estimation from liquid surface tension measurements. *Surface Science* **1977,** *62* (1), 267-276.

[31] Young, T., III. An essay on the cohesion of fluids. *Philosophical Transactions of the Royal Society of London* **1805,** *95*, 65-87.

[32] Fujiwara, H.; Collins, R. W., *Spectroscopic Ellipsometry for Photovoltaics: Volume 1: Fundamental Principles and Solar Cell Characterization*. Springer International Publishing: 2019.

[33] Tompkins, H.; Irene, E. A., *Handbook of Ellipsometry*. Elsevier Science: 2006.

[34] Hüfner, S., *Very High Resolution Photoelectron Spectroscopy*. Springer Berlin Heidelberg: 2007.

[35] Reinert, F.; Hüfner, S., Photoemission spectroscopy—from early days to recent applications. *New Journal of Physics* **2005,** *7*, 97-97.

[36] Kohli, R.; Mittal, K. L., *Developments in Surface Contamination and Cleaning - Vol 6: Methods of Cleaning and Cleanliness Verification*. Elsevier Science: 2013.

[37] Zou, Y.; Walton, A. S.; Kinloch, I. A.; Dryfe, R. A. W., Investigation of the Differential Capacitance of Highly Ordered Pyrolytic Graphite as a Model Material of Graphene. *Langmuir* **2016,** *32* (44), 11448-11455.

[38] Hurst, J. M.; Li, L.; Liu, H., Adventitious hydrocarbons and the graphite-water interface. *Carbon* **2018,** *134*, 464-469.

[39] Chen, R.; Nioradze, N.; Santhosh, P.; Li, Z.; Surwade, S. P.; Shenoy, G. J.; Parobek, D. G.; Kim, M. A.; Liu, H.; Amemiya, S., Ultrafast Electron Transfer Kinetics of Graphene Grown by Chemical Vapor Deposition. *Angewandte Chemie International Edition* **2015,** *54* (50), 15134-15137.

[40] Nioradze, N.; Chen, R.; Kurapati, N.; Khvataeva-Domanov, A.; Mabic, S.; Amemiya, S., Organic Contamination of Highly Oriented Pyrolytic Graphite As Studied by Scanning Electrochemical Microscopy. *Analytical Chemistry* **2015,** *87* (9), 4836-4843.

[41] Ajayan, P. M.; Tour, J. M., Nanotube composites. *Nature* **2007,** *447*, 1066.

[42] Nardelli, M. B.; Yakobson, B. I.; Bernholc, J., Brittle and Ductile Behavior in Carbon Nanotubes. *Physical Review Letters* **1998,** *81* (21), 4656-4659.

[43] Tamura, R.; Tsukada, M., Electronic states of the cap structure in the carbon nanotube. *Physical Review B* **1995,** *52* (8), 6015-6026.

[44] Qian, D.; Wagner, G. J.; Liu, W. K.; Yu, M.-F.; Ruoff, R. S., Mechanics of carbon nanotubes. *Applied Mechanics Reviews* **2002,** *55* (6), 495-533.

[45] Ru, C. Q., Effective bending stiffness of carbon nanotubes. *Physical Review B* **2000,** *62* (15), 9973-9976.

[46] Yakobson, B. I.; Brabec, C. J.; Bernholc, J., Nanomechanics of Carbon Tubes: Instabilities beyond Linear Response. *Physical Review Letters* **1996,** *76* (14), 2511-2514.

[47] Robertson, D. H.; Brenner, D. W.; Mintmire, J. W., Energetics of nanoscale graphitic tubules. *Physical Review B* **1992,** *45* (21), 12592-12595.

[48] Akinwande, D.; Brennan, C. J.; Bunch, J. S.; Egberts, P.; Felts, J. R.; Gao, H.; Huang, R.; Kim, J.-S.; Li, T.; Li, Y.; Liechti, K. M.; Lu, N.; Park, H. S.; Reed, E. J.; Wang, P.; Yakobson, B. I.; Zhang, T.; Zhang, Y.-W.; Zhou, Y.; Zhu, Y., A review on mechanics and mechanical properties of 2D materials—Graphene and beyond. *Extreme Mechanics Letters* **2017,** *13*, 42-77.

[49] Gorham, J. M.; Osborn, W. A.; Woodcock, J. W.; Scott, K. C. K.; Heddleston, J. M.; Hight Walker, A. R.; Gilman, J. W., Detecting carbon in carbon: Exploiting differential charging to obtain information on the chemical identity and spatial location of carbon nanotube aggregates in composites by imaging X-ray photoelectron spectroscopy. *Carbon* **2016,** *96*, 1208-1216.

[50] Zhang, Y.; Pan, C., Measurements of mechanical properties and number of layers of graphene from nano-indentation. *Diamond and Related Materials* **2012,** *24*, 1-5.

[51] Lee, J.-U.; Yoon, D.; Cheong, H., Estimation of Young's Modulus of Graphene by Raman Spectroscopy. *Nano Letters* **2012,** *12* (9), 4444-4448.

[52] Li, X. M.; Reinhoudt, D.; Crego-Calama, M., What do we need for a superhydrophobic surface? A review on the recent progress in the preparation of superhydrophobic surfaces. *Chem Soc Rev* **2007,** *36* (9), 1529-1529.

[53] Azimi, G.; Dhiman, R.; Kwon, H. M.; Paxson, A. T.; Varanasi, K. K., Hydrophobicity of rare-earth oxide ceramics. *Nature Materials* **2013,** *12* (4), 315-320.

[54] Preston, D. J.; Miljkovic, N.; Sack, J.; Enright, R.; Queeney, J.; Wang, E. N., Effect of hydrocarbon adsorption on the wettability of rare earth oxide ceramics. *Appl Phys Lett* **2014,** *105* (1).

[55] Luo, Y.; Li, J.; Zhu, J.; Zhao, Y.; Gao, X., Fabrication of Condensate Microdrop Self-Propelling Porous Films of Cerium Oxide Nanoparticles on Copper Surfaces. *Angewandte Chemie International Edition* **2015,** *54* (16), 4876-4879.

[56] Shi, Z.; Shum, P.; Zhou, Z.; Li, L. K.-Y., Effect of oxygen flow ratio on the wetting behavior, microstructure and mechanical properties of CeO2−x coatings prepared by magnetron sputtering. *Surface and Coatings Technology* **2017,** *320*, 333-338.

[57] Nakayama, K.; Hiraga, T.; Zhu, C.; Tsuji, E.; Aoki, Y.; Habazaki, H., Facile preparation of self-healing superhydrophobic CeO2 surface by electrochemical processes. *Applied Surface Science* **2017,** *423*, 968-976.

[58] Külah, E.; Marot, L.; Steiner, R.; Romanyuk, A.; Jung, T. A.; Wäckerlin, A.; Meyer, E., Surface chemistry of rare-earth oxide surfaces at ambient conditions: reactions with water and hydrocarbons. *Scientific Reports* **2017,** *7*, 43369.

[59] Lundy, R.; Byrne, C.; Bogan, J.; Nolan, K.; Collins, M. N.; Dalton, E.; Enright, R., Exploring the Role of Adsorption and Surface State on the Hydrophobicity of Rare Earth Oxides. *ACS Applied Materials & Interfaces* **2017,** *9* (15), 13751-13760.

[60] Kim, K. H.; Jahan, S. A.; Kabir, E.; Brown, R. J. C., A review of airborne polycyclic aromatic hydrocarbons (PAHs) and their human health effects. *Environ Int* **2013,** *60*, 71-80.

[61] Li, Z. T.; Wang, Y. J.; Kozbial, A.; Shenoy, G.; Zhou, F.; McGinley, R.; Ireland, P.; Morganstein, B.; Kunkel, A.; Surwade, S. P.; Li, L.; Liu, H. T., Effect of airborne contaminants on the wettability of supported graphene and graphite. *Nature Materials* **2013,** *12* (10), 925-931.

[62] Smith, T., The Hydrophilic Nature of a Clean Gold Surface. *Journal of Colloid and Interface Science* **1980,** *75* (1), 51-55.

[63] Shinozaki, A.; Arima, K.; Morita, M.; Kojima, I.; Azuma, Y., FTIR-ATR evaluation of organic contaminant cleaning methods for SiO2 surfaces. *Anal Sci* **2003,** *19* (11), 1557-1559.

[64] Hayun, S.; Ushakov, S. V.; Navrotsky, A., Direct Measurement of Surface Energy of CeO2 by Differential Scanning Calorimetry. *J Am Ceram Soc* **2011,** *94* (11), 3679-3682.

[65] Hayun, S.; Shvareva, T. Y.; Navrotsky, A., Nanoceria - Energetics of Surfaces, Interfaces and Water Adsorption. *J Am Ceram Soc* **2011,** *94* (11), 3992-3999.

[66] Gennard, S.; Cora, F.; Catlow, C. R. A., Comparison of the bulk and surface properties of ceria and zirconia by ab initio investigations. *J Phys Chem B* **1999,** *103* (46), 10158-10170.

[67] Kozbial, A.; Li, Z. T.; Conaway, C.; McGinley, R.; Dhingra, S.; Vahdat, V.; Zhou, F.; D'Urso, B.; Liu, H. T.; Li, L., Study on the Surface Energy of Graphene by Contact Angle Measurements. *Langmuir* **2014,** *30* (28), 8598-8606.

[68] Khan, S.; Azimi, G.; Yildiz, B.; Varanasi, K. K., Role of surface oxygen-to-metal ratio on the wettability of rare-earth oxides. *Appl Phys Lett* **2015,** *106* (6).

[69] Raj, R.; Maroo, S. C.; Wang, E. N., Wettability of graphene. *Nano Letters* **2013,** *13* (4), 1509-15.

[70] Stando, G.; Łukawski, D.; Lisiecki, F.; Janas, D., Intrinsic hydrophilic character of carbon nanotube networks. *Applied Surface Science* **2019,** *463*, 227-233.

[71] Kozbial, A.; Li, Z.; Sun, J.; Gong, X.; Zhou, F.; Wang, Y.; Xu, H.; Liu, H.; Li, L., Understanding the intrinsic water wettability of graphite. *Carbon* **2014,** *74* (Supplement C), 218-225.

[72] Kozbial, A.; Li, Z.; Conaway, C.; McGinley, R.; Dhingra, S.; Vahdat, V.; Zhou, F.; D'Urso, B.; Liu, H.; Li, L., Study on the Surface Energy of Graphene by Contact Angle Measurements. *Langmuir* **2014,** *30* (28), 8598-8606.

[73] Kozbial, A.; Trouba, C.; Liu, H.; Li, L., Characterization of the Intrinsic Water Wettability of Graphite Using Contact Angle Measurements: Effect of Defects on Static and Dynamic Contact Angles. *Langmuir* **2017,** *33* (4), 959-967.

[74] Li, Z.; Kozbial, A.; Nioradze, N.; Parobek, D.; Shenoy, G. J.; Salim, M.; Amemiya, S.; Li, L.; Liu, H., Water Protects Graphitic Surface from Airborne Hydrocarbon Contamination. *ACS Nano* **2016,** *10* (1), 349-359.

[75] Young, M. J.; Musgrave, C. B.; George, S. M., Growth and Characterization of Al2O3 Atomic Layer Deposition Films on sp2-Graphitic Carbon Substrates Using NO2/Trimethylaluminum Pretreatment. *ACS Applied Materials & Interfaces* **2015,** *7* (22), 12030-12037.

[76] Aria, A. I.; Nakanishi, K.; Xiao, L.; Braeuninger-Weimer, P.; Sagade, A. A.; Alexander-Webber, J. A.; Hofmann, S., Parameter Space of Atomic Layer Deposition of Ultrathin Oxides on Graphene. *ACS Applied Materials & Interfaces* **2016,** *8* (44), 30564-30575.

[77] Martinez-Martin, D.; Longuinhos, R.; Izquierdo, J. G.; Marele, A.; Alexandre, S. S.; Jaafar, M.; Gómez-Rodríguez, J. M.; Bañares, L.; Soler, J. M.; Gomez-Herrero, J., Atmospheric contaminants on graphitic surfaces. *Carbon* **2013,** *61*, 33-39.

[78] Temiryazev, A.; Frolov, A.; Temiryazeva, M., Atomic-force microscopy study of self-assembled atmospheric contamination on graphene and graphite surfaces. *Carbon* **2019,** *143*, 30-37.

[79] Choong, S. W.; Russell, S. R.; Bang, J. J.; Patterson, J. K.; Claridge, S. A., Sitting Phase Monolayers of Polymerizable Phospholipids Create Dimensional, Molecular-Scale Wetting Control for Scalable Solution-Based Patterning of Layered Materials. *ACS Applied Materials & Interfaces* **2017,** *9* (22), 19326-19334.

[80] Sommerhalter, C.; Matthes, T. W.; Glatzel, T.; Jäger-Waldau, A.; Lux-Steiner, M. C., High-sensitivity quantitative Kelvin probe microscopy by noncontact ultra-high-vacuum atomic force microscopy. *Appl Phys Lett* **1999,** *75* (2), 286-288.

[81] Fellner-Feldegg, H.; Gelius, U.; Wannberg, B.; Nilsson, A. G.; Basilier, E.; Siegbahn, K., New developments in ESCA-instrumentation. *Journal of Electron Spectroscopy and Related Phenomena* **1974,** *5* (1), 643-689.

[82] Siegbahn, K., Electron spectroscopy - an outlook. *Journal of Electron Spectroscopy and Related Phenomena* **1974,** *5* (1), 3-97.

[83] Penchina, C. M.; Sapp, E.; Tejeda, J.; Shevchik, N., Photoemission spectra from conduction bands and core levels of sputter-deposited tungsten films. *Physical Review B* **1974,** *10* (10), 4187-4194.

[84] Salaneck, W. R., Intermolecular Relaxation Effects in the Ultraviolet Photoelectron Spectroscopy of Molecular Solids. In *Photon, Electron, and Ion Probes of Polymer Structure and Properties*, American Chemical Society: 1981; Vol. 162, pp 121-149.

[85] Susi, T.; Pichler, T.; Ayala, P., X-ray photoelectron spectroscopy of graphitic carbon nanomaterials doped with heteroatoms. *Beilstein Journal of Nanotechnology* **2015,** *6*, 177-192.

[86] Tanuma, S.; Shiratori, T.; Kimura, T.; Goto, K.; Ichimura, S.; Powell, C. J., Experimental determination of electron inelastic mean free paths in 13 elemental solids in the 50 to 5000 eV energy range by elastic-peak electron spectroscopy. *Surface and Interface Analysis* **2005,** *37* (11), 833-845.

[87] Angus, J. C., Categorization of Dense Hydrocarbon Films. In *Amorphous Hydrogenated Carbon Films XVII*, Koidl, P.; Oelhafen, P., Eds. Strasbourg, France, 1987; Vol. XVII, pp 179-187.

[88] Robertson, J.; O'Reilley, E. P., The Electronic Strucutre of a-C:H. In *Amorphous Hydrogenated Carbon Films XVII*, Strasbourg, France, 1987; pp 251-258.

[89] Oelhafen, P.; Ugolini, D., Photoelectron Spectroscopy Measurements on In-situ Prepared a-C:H Films. In *Amorphous Hydrogenated Carbon Films XVII*, Koidl, P.; Oelhafen, P., Eds. Strasbourg, France, 1987; pp 267-273.

[90] Savvides, N., Low-Energy Ion-Assisted Deposition of a-C:H films: A Study of Optical Parameters with Increasing Hydrogenation. In *Amorphous Hydrogenated Carbon Films XVII*, Koidl, P.; Oelhafen, P., Eds. Strasbourg, France, 1987; pp 275-284.

[91] Ugolini, D.; Eitle, J.; Oelhafen, P., Electron-Spectroscopy Measurements on Hydrogen Implanted Graphite and Comparison to Amorphous Hydrogenated Carbon-Films (a-C-H). *Appl Phys a-Mater* **1992,** *54* (1), 57-60.

[92] Ugolini, D.; Eitle, J.; Oelhafen, P., Influence of Process Gas and Deposition Energy on the Atomic and Electronic-Structure of Diamond-Like (a-C-H) Films. *Vacuum* **1990,** *41* (4-6), 1374-1377.

[93] Ugolini, D.; Oelhafen, P.; Wittmer, M., Characterization of a-C:H/Substrate Interfaces by Electron Spectroscopy Measurements. I : Metallic Substrates. In *Amorphous Hydrogenated Carbon Films XVII*, Koidl, P.; Oelhafen, P., Eds. Strasbourg, France, 1987; pp 297-303.

[94] Schelz, S.; Eitle, J.; Steiner, R.; Oelhafen, P., In situ electron spectroscopy on polymeric films prepared by RF plasma polymerization: styrene and hydrogen/styrene gas mixtures as process gases. *Applied Surface Science* **1991,** *48-49* (Supplement C), 301-306.

[95] Hossain, M. Z.; Johns, J. E.; Bevan, K. H.; Karmel, H. J.; Liang, Y. T.; Yoshimoto, S.; Mukai, K.; Koitaya, T.; Yoshinobu, J.; Kawai, M.; Lear, A. M.; Kesmodel, L. L.; Tait, S. L.; Hersam, M. C., Chemically homogeneous and thermally reversible oxidation of epitaxial graphene. *Nature Chemistry* **2012,** *4*, 305-309.

[96] Bianconi, A.; Hagstrom, S. B. M.; Bachrach, R. Z., Photoemission Studies of Graphite High-Energy Conduction-Band and Valence-Band States Using Soft-X-Ray Synchrotron Radiation Excitation. *Physical Review B* **1977,** *16* (12), 5543-5548.

[97] Cakir, P.; Eloirdi, R.; Huber, F.; Konings, R. J. M.; Gouder, T., Surface Reduction of Neptunium Dioxide and Uranium Mixed Oxides with Plutonium and Thorium by Photocatalytic Reaction with Ice. *J Phys Chem C* **2015,** *119* (3), 1330-1337.

[98] Hagsteöm, A. L.; Platau, A.; Kaelsson, S. E., Adsorption of oxygen at room temperature on polycrystalline titanium studied by ultraviolet and X-ray photoelectron spectroscopy. *physica status solidi (b)* **1977,** *83* (1), 77-84.

[99] Krischok, S.; Höfft, O.; Günster, J.; Stultz, J.; Goodman, D. W.; Kempter, V., H2O interaction with bare and Li-precovered TiO2: studies with electron spectroscopies (MIES and UPS(HeI and II)). *Surface Science* **2001,** *495* (1), 8-18.

[100] Kurtz, R. L.; Stockbauer, R.; Madey, T. E.; Mueller, D.; Shih, A.; Toth, L., Initial Stages of degredation of superconductor surfaces: O2, H2O, CO2, and CO chemisorption on La2-xSrxCuO4. *Physical Review B* **1988,** *37* (13), 7936-7939.

[101] Bahr, S.; Borodin, A.; Hofft, O.; Kempter, V.; Allouche, A.; Borget, F.; Chiavassa, T., Interaction of acetic acid with solid water. *J Phys Chem B* **2006,** *110* (17), 8649-8656.

[102] Günster, J.; Krischok, S.; Stultz, J.; Goodman, D. W., Interaction of Na with Multilayer Water on MgO(100). *The Journal of Physical Chemistry B* **2000,** *104* (33), 7977-7980.

[103] Yashonath, S.; Basu, P. K.; Srinivasan, A.; Hedge, M. S.; Rao, C. N. R., Photoelectron spectroscopic studies of the adsorption of organic molecules with lone pair orbitals on transition metal surfaces. *Proceedings of the Indian Academy of Sciences - Chemical Sciences* **1982,** *91* (2), 101-128.

[104] Page, P. J.; Williams, P. M., Ultra-violet photoelectron spectroscopy studies of gas adsorption on transition metals. *Faraday Discussions of the Chemical Society* **1974,** *58* (0), 80-89.

[105] Keil, M.; Samorí, P.; dos Santos, D. A.; Kugler, T.; Stafström, S.; Brand, J. D.; Müllen, K.; Brédas, J. L.; Rabe, J. P.; Salaneck, W. R., Influence of the Morphology on the Electronic Structure of Hexa-peri-hexabenzocoronene Thin Films. *The Journal of Physical Chemistry B* **2000,** *104* (16), 3967-3975.

[106] Brédas, J. L.; Street, G. B., Electronic Strucutre of Amorphous Hydrogenated Carbon Films: Theoretical Invenstigations on Model Compounds. In *Amorphous Hydrogenated Carbon Films XVII*, Strasbourg, France, 1987; pp 237-250.

[107] Himpsel, F. J.; van der Veen, J. F.; Eastman, D. E., Experimental bulk energy bands for diamond usinghν-dependent photoemission. *Physical Review B* **1980,** *22* (4), 1967-1971.

[108] Dischler, B., Bonding and Hydrogen Incorporation in a-C:H studied by Infrared Spectroscopy. In *Amorphous Hydrogenated Carbon Films XVII*, Koidl, P.; Oelhafen, P., Eds. Strasbourg, France, 1987; pp 189-201.

[109] Brundle, C. R.; Carley, A. F., XPS and UPS studies of the adsorption of small molecules on polycrystalline Ni films. *Faraday Discussions of the Chemical Society* **1975,** *60* (0), 51-70.

[110] Bukhtiyarov, V. I.; Kaichev, V. V.; Podgornov, E. A.; Prosvirin, I. P., XPS, UPS, TPD and TPR studies of oxygen species active in silver-catalysed ethylene epoxidation. *Catalysis Letters 57* (1999), 233-239.

[111] WEINBERG, T. E. F. a. W. H., An XPS and UPS Study of the Kinetics of Carbon Monoxide-De Oxidation Over Ag(111). *Surface Science 118* (1982), 369-386.

[112] Plummer, E. W.; Eberhardt, W., Angle-Resolved Photoemission as a Tool for the Study of Surfaces. In *Advances in Chemical Physics*, John Wiley & Sons, Inc.: 2007; pp 533-656.

[113] Miranda, R.; Wandelt, K.; Rieger, D.; Schnell, R. D., Angle-resolved photoemission of CO chemisorption on Pd(111). *Surface Science* **1984,** *139* (2), 430-442.

[114] Zhou, S. Y.; Gweon, G. H.; Spataru, C. D.; Graf, J.; Lee, D. H.; Louie, S. G.; Lanzara, A., Coexistence of sharp quasiparticle dispersions and disorder features in graphite. *Physical Review B* **2005,** *71* (16), 161403.

[115] Law, A. R.; Johnson, M. T.; Hughes, H. P., Synchrotron-radiation-excited angle-resolved photoemission from single-crystal graphite. *Physical Review B* **1986,** *34* (6), 4289-4297.

[116] Mansour, A.; Oelhafen, P., Effects of defects on the electronic structure of ion-irradiated graphite. *Applied Physics A* **1994,** *58* (5), 437-440.

[117] Calliari, L.; Speranza, G.; Santoni, A., The graphite Valence Band electronic structure: a combined Core–Valence–Valence Auger and Valence Band photoemission study. *Journal of Electron Spectroscopy and Related Phenomena* **2002,** *127* (1), 125-130.

[118] Li, H.; Schlögl, R.; Risse, T. Determination of Oxygen Functionality on Highly Oriented Pyrolytic Graphite (HOPG). FU Berlin, 2012.

[119] Law, A. R.; Barry, J. J.; Hughes, H. P., Angle-resolved photoemission and secondary electron emission from single-crystal graphite. *Physical Review B* **1983,** *28* (9), 5332-5335.

[120] Smith, R. S.; May, R. A.; Kay, B. D., Desorption Kinetics of Ar, Kr, Xe, N2, O2, CO, Methane, Ethane, and Propane from Graphene and Amorphous Solid Water Surfaces. *The Journal of Physical Chemistry B* **2016,** *120* (8), 1979-1987.

[121] Castro, M. A.; Clarke, S. M.; Inaba, A.; Arnold, T.; Thomas, R. K., Competitive Adsorption of Simple Linear Alkane Mixtures onto Graphite. *The Journal of Physical Chemistry B* **1998,** *102* (51), 10528-10534.

[122] Müller, T.; Flynn, G. W.; Mathauser, A. T.; Teplyakov, A. V., Temperature-Programmed Desorption Studies of n-Alkane Derivatives on Graphite: Desorption Energetics and the Influence of Functional Groups on Adsorbate Self-Assembly. *Langmuir* **2003,** *19* (7), 2812-2821.

[123] Gellman, A. J.; Paserba, K. R., Kinetics and Mechanism of Oligomer Desorption from Surfaces: n-Alkanes on Graphite. *The Journal of Physical Chemistry B* **2002,** *106* (51), 13231-13241.

[124] Kawashima, Y.; Iwamoto, M., Protolytic decomposition of n-octane on graphite at near room temperature. *Scientific Reports* **2016,** *6*, 28493.

[125] Clemens, A.; Hellberg, L.; Gronbeck, H.; Chakarov, D., Water desorption from nanostructured graphite surfaces. *Physical Chemistry Chemical Physics* **2013,** *15* (47), 20456-20462.

[126] Marchon, B.; Carrazza, J.; Heinemann, H.; Somorjai, G. A., TPD and XPS studies of O2, CO2, and H2O adsorption on clean polycrystalline graphite. *Carbon* **1988,** *26* (4), 507-514.

[127] Kwon, S.; Vidic, R.; Borguet, E., The effect of surface chemical functional groups on the adsorption and desorption of a polar molecule, acetone, from a model carbonaceous surface, graphite. *Surface Science* **2003,** *522* (1), 17-26.

[128] Ishiwari, S.; Kato, H.; Habukac, H., Development of Evaluation Method for Organic Contamination on Silicon Wafer Surfaces. *J. Electrochem. Soc.* **2001,** *148* (11), G644-G648.

[129] Ye, S.; Ichihara, T.; Uosaki, K., Attenuated total reflection Fourier transform infrared spectroscopy study of the adsorption of organic contaminants on a hydrogen-terminated Si(111) surface in air. *Appl Phys Lett* **1999,** *75* (11), 1562-1564.

[130] Saito, M. Proceedings of the 1995 International Symposium on Semiconductor Manufacturing, The Ultra Clean Society, Tokyo, Tokyo, 1995; p 171.

[131] Tlili, S.; Gómez Alvarez, E.; Gligorovski, S.; Wortham, H., Adsorption behavior of two model airborne organic contaminants on wafer surfaces. *Chemical Engineering Journal* **2012,** *187* (Supplement C), 239-247.

[132] Chen, R.; Balla, R. J.; Li, Z.; Liu, H.; Amemiya, S., Origin of Asymmetry of Paired Nanogap Voltammograms Based on Scanning Electrochemical Microscopy: Contamination Not Adsorption. *Analytical Chemistry* **2016,** *88* (16), 8323-8331.

[133] Zhao, Q.; Nardelli, M. B.; Bernholc, J., Ultimate strength of carbon nanotubes: A theoretical study. *Physical Review B* **2002,** *65* (14), 144105.

[134] Cao, G., Atomistic Studies of Mechanical Properties of Graphene. *Polymers* **2014,** *6* (9), 2404.

[135] Yu, M.-F.; Lourie, O.; Dyer, M. J.; Moloni, K.; Kelly, T. F.; Ruoff, R. S., Strength and Breaking Mechanism of Multiwalled Carbon Nanotubes Under Tensile Load. *Science* **2000,** *287* (5453), 637-640.

[136] Lee, C.; Wei, X.; Kysar, J. W.; Hone, J., Measurement of the Elastic Properties and Intrinsic Strength of Monolayer Graphene. *Science* **2008,** *321* (5887), 385-388.

[137] Papageorgiou, D. G.; Kinloch, I. A.; Young, R. J., Mechanical properties of graphene and graphene-based nanocomposites. *Progress in Materials Science* **2017,** *90*, 75-127.

[138] Potts, J. R.; Dreyer, D. R.; Bielawski, C. W.; Ruoff, R. S., Graphene-based polymer nanocomposites. *Polymer* **2011,** *52* (1), 5-25.

[139] Wong, E. W.; Sheehan, P. E.; Lieber, C. M., Nanobeam Mechanics: Elasticity, Strength, and Toughness of Nanorods and Nanotubes. *Science* **1997,** *277* (5334), 1971-1975.

[140] Yu, M.-F.; Files, B. S.; Arepalli, S.; Ruoff, R. S., Tensile Loading of Ropes of Single Wall Carbon Nanotubes and their Mechanical Properties. *Physical Review Letters* **2000,** *84* (24), 5552-5555.

[141] Pan, Z. W.; Xie, S. S.; Lu, L.; Chang, B. H.; Sun, L. F.; Zhou, W. Y.; Wang, G.; Zhang, D. L., Tensile tests of ropes of very long aligned multiwall carbon nanotubes. *Applied Physics Letters* **1999,** *74* (21), 3152-3154.

[142] Li, Y.; Wang, K.; Wei, J.; Gu, Z.; Wang, Z.; Luo, J.; Wu, D., Tensile properties of long aligned double-walled carbon nanotube strands. *Carbon* **2005,** *43* (1), 31-35.

[143] Zhu, H. W.; Xu, C. L.; Wu, D. H.; Wei, B. Q.; Vajtai, R.; Ajayan, P. M., Direct Synthesis of Long Single-Walled Carbon Nanotube Strands. *Science* **2002,** *296* (5569), 884-886.

[144] Griffith, A. A.; Taylor, G. I., VI. The phenomena of rupture and flow in solids. *Philosophical Transactions of the Royal Society of London. Series A, Containing Papers of a Mathematical or Physical Character* **1921,** *221* (582-593), 163-198.

[145] Banhart, F.; Kotakoski, J.; Krasheninnikov, A. V., Structural Defects in Graphene. *ACS Nano* **2011,** *5* (1), 26-41.

[146] Li, X. S.; Cai, W. W.; An, J. H.; Kim, S.; Nah, J.; Yang, D. X.; Piner, R.; Velamakanni, A.; Jung, I.; Tutuc, E.; Banerjee, S. K.; Colombo, L.; Ruoff, R. S., Large-Area Synthesis of High-Quality and Uniform Graphene Films on Copper Foils. *Science* **2009,** *324* (5932), 1312-1314.

[147] Chen, S. S.; Ji, H. X.; Chou, H.; Li, Q. Y.; Li, H. Y.; Suk, J. W.; Piner, R.; Liao, L.; Cai, W. W.; Ruoff, R. S., Millimeter-Size Single-Crystal Graphene by Suppressing Evaporative Loss of Cu During Low Pressure Chemical Vapor Deposition. *Advanced Materials* **2013,** *25* (14), 2062-2065.

[148] Ferrari, A. C.; Meyer, J. C.; Scardaci, V.; Casiraghi, C.; Lazzeri, M.; Mauri, F.; Piscanec, S.; Jiang, D.; Novoselov, K. S.; Roth, S.; Geim, A. K., Raman spectrum of graphene and graphene layers. *Physical Review Letters* **2006,** *97* (18).

[149] Graf, D.; Molitor, F.; Ensslin, K.; Stampfer, C.; Jungen, A.; Hierold, C.; Wirtz, L., Spatially resolved raman spectroscopy of single- and few-layer graphene. *Nano Letters* **2007,** *7* (2), 238-242.

[150] Witkowski, A.; Stec, A. A.; Hull, T. R., Thermal Decomposition of Polymeric Materials. In *SFPE Handbook of Fire Protection Engineering*, Hurley, M. J.; Gottuk, D.; Hall, J. R.; Harada, K.; Kuligowski, E.; Puchovsky, M.; Torero, J.; Watts, J. M.; Wieczorek, C., Eds. Springer New York: New York, NY, 2016; pp 167-254.

[151] Ferriol, M.; Gentilhomme, A.; Cochez, M.; Oget, N.; Mieloszynski, J. L., Thermal degradation of poly(methyl methacrylate) (PMMA): modelling of DTG and TG curves. *Polymer Degradation and Stability* **2003,** *79* (2), 271-281.

[152] Hwangbo, Y.; Lee, C.-K.; Kim, S.-M.; Kim, J.-H.; Kim, K.-S.; Jang, B.; Lee, H.-J.; Lee, S.-K.; Kim, S.-S.; Ahn, J.-H.; Lee, S.-M., Fracture Characteristics of Monolayer CVD-Graphene. *Scientific Reports* **2014,** *4*, 4439.